Nucleic Acids Research, 2025, **53**, gkaf539
https://doi.org/10.1093/nar/gkaf539
Gene regulation, Chromatin and Epigenetics

The lincRNA *Pantr1* is a FOXG1 target gene conferring site-specific chromatin binding of FOXG1

Fabian Gather[1,†], Tudor Rauleac[1,†], Ipek Akol[1,†], Ganeshkumar Arumugam[1,2], Camila L. Fullio[1,3], Teresa Müller[4], Dimitrios Kleidonas[2,3,5], Ruth Geiss-Friedlander[6], Andre Fischer[7,8,9], Andreas Vlachos[5,10], Rolf Backofen[4,11], Tanja Vogel[1,*]

[1]Institute for Anatomy and Cell Biology, Department of Molecular Embryology, Faculty of Medicine, Albert-Ludwigs-University Freiburg, 79104 Freiburg, Germany
[2]Spemann Graduate School of Biology and Medicine (SGBM), Albert-Ludwigs-University Freiburg, 79104 Freiburg, Germany
[3]Faculty of Biology, Albert-Ludwigs-University Freiburg, 79104 Freiburg, Germany
[4]Bioinformatics Group, Department of Computer Science, Albert-Ludwigs-University Freiburg, 79110 Freiburg, Germany
[5]Institute for Anatomy and Cell Biology, Department of Neuroanatomy, Faculty of Medicine, Albert-Ludwigs-University Freiburg, 79104 Freiburg, Germany
[6]Institute for Molecular Medicine and Cell Research, Center of Biochemistry and Molecular Cell Research (ZBMZ), Faculty of Medicine, Albert-Ludwigs-University Freiburg, 79110 Freiburg, Germany
[7]Department for Systems Medicine and Epigenetics, German Center for Neurodegenerative Diseases (DZNE), 37075 Göttingen, Germany
[8]Cluster of Excellence "Multiscale Bioimaging: from Molecular Machines to Networks of Excitable Cells" (MBExC), University of Göttingen, 37075 Göttingen, Germany
[9]Department of Psychiatry and Psychotherapy, University Medical Center Göttingen, 37075 Göttingen, Germany
[10]Center BrainLinks-BrainTools, Albert-Ludwigs-University Freiburg, 79110 Freiburg, Germany
[11]Signalling Research Centres BIOSS and CIBSS, Albert-Ludwigs-University of Freiburg, 79104 Freiburg, Germany

[*]To whom correspondence should be addressed. Email: tanja.vogel@anat.uni-freiburg.de
[†]The first three authors should be regarded as Joint First Authors.

Abstract

Derailed gene expression programs within the developing nervous system, encompassing both transcriptional and post-transcriptional processes, can cause diverse neurodevelopmental diseases (NDD). The NDD FOXG1-syndrome lacks full understanding of the mechanistic role of its eponymous gene product. While it is known that FOXG1 acts in part at the chromatin by binding to regulative regions, it is unclear what factors control its presence at specific sites. Long non-coding RNAs (lncRNAs) can mediate site-directed transcription factor binding, but their potential role in FOXG1-syndrome has not been described. Here, we show that FOXG1 localisation is regulated at selected loci through the lncRNA *Pantr1*. We identified FOXG1 as an upstream transcriptional activator of *Pantr1* in human and mice. Further, we discovered that FOXG1 has the ability to associate with RNAs. Both transcriptional regulation of *Pantr1* by FOXG1 and binding of both partners build up a regulative network that impacts the localisation of FOXG1 at selected genomic loci. Specifically, *Pantr1* facilitates cooperative presence of FOXG1/NEUROD1 at specific sites, and *Pantr1* reduction leads to redistribution of FOXG1 to comparably more generic binding sites. The rescue of impaired dendritic outgrowth upon FOXG1 reduction by simultaneous overexpression of *Pantr1* underlines the importance of the FOXG1/*Pantr1* regulative network.

Graphical abstract

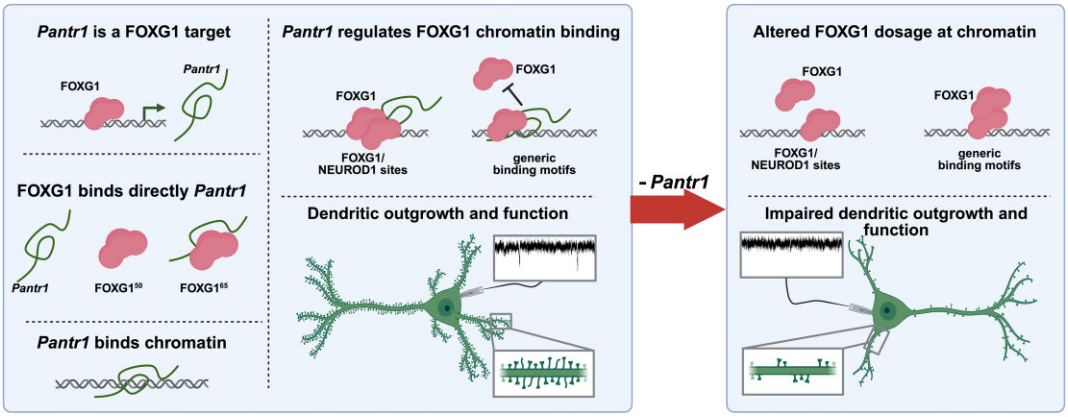

Received: October 8, 2024. **Revised:** April 30, 2025. **Editorial Decision:** May 20, 2025. **Accepted:** June 2, 2025

Introduction

Forkhead box G1 (FOXG1)-syndrome (OMIM 613454) is a rare, congenital form in the Rett- and autism-spectrum disorders. Patients with *FOXG1* mutations present with a complex phenotypic spectrum [1], caused at least in part by impaired neuronal networks and functions. FOXG1's link to autism is established both in humans [2] and mice [3]. In mice, FOXG1 plays a central role in forebrain development as its complete absence results in anencephaly [4]. It influences proliferation as well as differentiation of neural stem cells and is involved in the migration and integration of pyramidal neurons into the cortical plate [5–7]. FOXG1 prevents neural stem cells from premature differentiation, thereby maintaining the number of progenitors available for the generation of specific neuronal subtypes. Accordingly, overexpression (OE) of FOXG1 increases the stem cell pool and delays neurogenesis [8]. Moreover, FOXG1 expression inhibits differentiation of Cajal-Retzius-cells, which are overabundant in FOXG1-deficient forebrains [9], and FOXG1 deficiency impairs proper development of the ventral telencephalon through altered expression of ventralising signals [10].

FOXG1 also impacts the postnatal brain function. In the mouse postnatal hippocampus, for example, FOXG1 is involved in the proper development of the dentate gyrus. Here, it maintains the balance between proliferation and differentiation of both neurons and glia cells [11], similar to that of cortical stem cells [8]. Additionally, loss of FOXG1 results in increased cell death of postmitotic neurons in the hippocampus and cerebellum [11, 12]. Reduced levels of FOXG1 in the hippocampus further impact the animal's behaviour. *Foxg1*-haploinsufficient mice are hyperactive, and they perform less well in contextual fear conditioning compared to wild-type controls [13]. Recent studies show altered electrophysiological properties upon reduced or increased FOXG1 levels, dysbalanced neuronal functions of excitation and inhibition as important basis for impaired behaviour, reduced dendritic complexity and reduced spine densities, both in the cortex and hippocampus [3, 14–17].

The molecular functions of FOXG1 are becoming increasingly recognised. FOXG1 prevents cell cycle exit of progenitor cells and promotes stem cell pool expansion by repressing the expression of *Cdkn1a* [18, 19]. In this setting, FOXG1 sponges FOXO/SMAD complexes and prevents their binding to regulative sites, which normally activate *Cdkn1a* expression. Thereby, FOXG1 antagonises FOXO/SMAD-dependent neuronal differentiation of cortical progenitors [20]. An increasing number of studies report FOXG1 binding to chromatin and suggest potential direct chromatin-related functions [6, 7, 21, 22]. These functions impact gene expression programmes that are implicated in neuronal differentiation and confer layer identity through its presence at a monomethylated histone H3 lysine 4 (H3K4me1) enhancer of the cortical layer 4 gene *Nr2f1*, which is kept in a repressed state. Removal of FOXG1 in projection neurons activates *Nr2f1* and a layer 4 neuron-specific transcriptional program [6]. In addition, FOXG1 regulates callosal axon guidance and neuronal migration by acting within a FOXG1/ZBTB18 complex that directly binds and represses *Robo1*, *Slit3*, and *Reelin* genes [7].

While chromatin immunoprecipitation sequencing (ChIPseq) data reveal FOXG1's utilisation of diverse modalities to bind to chromatin and alter the epigenetic and transcriptional landscape [22], the mechanism underlying FOXG1's chromatin targeting remains elusive. Even though FOXG1 binds a common Forkhead (Fkh)-recognised consensus sequence (5′-RYAAAYA-3′) [23], ChIPseq data suggest that FOXG1 or complexes containing FOXG1 associate with alternative sequences as well [22]. Here, non-coding RNAs might confer sequence-specific recruitment of FOXG1. Despite the fact that specific microRNAs are involved in FOXG1-syndrome [24], it is not yet reported whether other non-coding RNAs, especially long (intergenic) non-coding RNAs (l(i)ncRNAs) contribute to this neurodevelopment disorder. This study unravels lincRNA, i.e. POU3F3 Adjacent Non-Coding Transcript 1 (*Pantr1),* contribution to FOXG1-syndrome, in both human and mouse model systems. We demonstrate that *Pantr1* is a direct target of FOXG1 and reveal a novel mechanism by which FOXG1 binding to specific chromatin regions is influenced by its association with *Pantr1*. Notably, the OE of *Pantr1* rescued dendritic outgrowth defects resulting from reduced FOXG1 expression. Our findings thus underscore the crucial role of the lincRNA *Pantr1* in FOXG1-mediated neuronal differentiation and function.

Material and methods

All reagents are listed in Table 1.

Organoid culture

Human induced pluripotent stem cell (hiPSC) lines were grown in mTESR1 medium (Stem Cell, Canada) on Matrigel (Corning, USA). Control hiPSCs (FiPS Core, University Medicine Freiburg, Germany) were generated from fibroblast of a healthy donor (HD) [25]. FOXG1del and FOXG1c460 hiPSCs were obtained from the Telethon, University of Siena (code 611/2013 #5) [17]. Human cerebral organoids (hCO) were generated according to an adapted version of the standard protocol [26], as described [27]. Briefly, 35 000 cells per well were seeded into V-shaped, non-coated 96-well plates, centrifuged, and treated as described. Organoids were cultivated in organoid medium up to day (d) 105, counted from the day of transfer into spinning bottles. Half of the medium was exchanged once per week until week 10 and twice per week thereafter. After 105 days of cultivation, two organoids derived from control, FOXG1del and FOXG1c460 hiPSCs, were further processed for scRNAseq libraries. For quantitative real-time PCR (qPCR), single organoids represented individual biological replicates (n); organoids were not pooled.

Mice

Foxg1$^{cre/+}$ and *Foxg1*$^{cre/cre}$ mice were maintained in a C57Bl/6 background are described by the producers [28], (https://www.jax.org/strain/004337). As multiple recent studies have not shown any discernible sex difference in heterozygote *Foxg1* mouse models [7, 13, 29, 30], in this study, mice were not segregated based on sex. Wild-type mice (C57BL/6J, NMRI or CD1) were obtained from Charles River, Germany, or Janvier, France.

Mouse tissue isolation for RNAseq

Cortices of E13.5 embryos were dissected from *Foxg1*$^{cre/cre}$ and wild-type mice (*Foxg1*$^{+/+}$), hippocampi of E18.5 embryos,

Table 1. Reagents

Name	Catalog number	Company	Location
2-Mercaptoethanol 50mM	31350–010	Gibco, Thermo Scientific	USA
Accutase	A1110501	Gibco, Thermo Scientific	USA
Albumin Fraktion V	8076.4	Roth	Germany
Anti-adherence rinsing solution	7010	STEMCELL	Canada
AraC	C1768	Sigma-Aldrich/Merck	Germany
B-27 Supplement (50x) 10ml	17504–044	Gibco, Thermo Scientific	USA
Bradford reagent	5 000 006	Bio-Rad	United Kingdom
BSA	8076.4	Roth	Germany
Chromium Next GEM Single Cell 3′ Reagent Kits v3.1	PN-1 000 121	10X Genomics	CA, USA
DAPI	D9542	Sigma-Aldrich/Merck	Germany
DMEM (high glucose)	11960–044	Gibco, Thermo Scientific	USA
DMEM/NUT.MIX F-12 W/GLUT-I	31 331 028	Thermo Scientific	USA
DNAse digestion	79 254	Qiagen	Germany
DPBS	14190–094	Gibco	United Kingdom
EDTA	AM9260G	Thermo Scientific	USA
Fetal bovine serum	10500–064	Gibco, Thermo Scientific	USA
Fluorescent mounting medium	S3023	DAKO, Agilent	USA
Formaldehyde	252 549	Sigma-Aldrich/Merck	Germany
Formamide	F9037	Sigma-Aldrich	Germany
GelRed nucleic acid gel stain, 10 000X	#41 003	Biotium	USA
Glycine	3908.3	Roth	Germany
GoTaq® qPCR Master Mix	A6002	Promega	WI, USA
Hanks' Balanced Salt Solution (HBSS)	14 025	Gibco, Thermo Scientific	Germany
Hs-PANTR1	1 199 961	Bio-Techne	Germany
Insulin human	11 376 497 001	Sigma-Aldrich/Merck	Germany
Laminin	L2020-1MG	Sigma-Aldrich/Merck	Germany
L-glutamine	25 030 081	Gibco, Thermo Scientific	USA
Matrigel	354 277	Corning	USA
MEM NEAA	11140–035	Gibco, Thermo Scientific	USA
Mirus TransIT-293 Transfection Reagent	MIRUMIR2700	Mirus Bio LLC	USA
Mm-Pantr1	483 711	Bio-Techne	Germany
mTESR1 medium	85 850	Stem Cell	Canada
N2-Supplement	17 502 048	Gibco, Thermo Scientific	USA
NaCl	92 652	Roth	Germany
NEUROBASAL MED SFM	21 103 049	Thermo Fisher	USA
Nonidet-40, NP-40 Alternative	492 016	Calbiochem	USA
Normal donkey serum	017–000-121	Jackson Immuno Research	United Kingdom
Normal goat serum	G6767	Sigma-Aldrich/Merck	Germany
Not1	R0189S	New England Biolabs	USA
OPTIMEM	31985–062	Gibco, Thermo Scientific	USA
PageRuler™ Prestained Protein Ladder, 10 to 180 kDa	26 616	Thermo Scientific	USA
Papain Dissociation System	LK003150	Worthington	USA
Penicillin-Streptomycin	15 140 122	Gibco, Thermo Scientific	USA
PFA	MC1040051000	Sigma-Aldrich/Merck	Germany
Pierce™ Magnetic RNA-Protein Pull-Down Kit	20 164	Thermo Scientific	USA
Pierce™ RNA 3′ End Desthiobiotinylation Kit	20 163	Thermo Scientific	USA
Pierce Sterptavidin Magnetic Beads	88 816	Thermo Scientific	USA
PORN Poly-L- ornithine hydro	P3655-100MG	Sigma-Aldrich/Merck	Germany
PMSF (Phenylmethylsulfonyl fluoride)	10 837 091 001	Merck	Germany
Primers (see Table 3)		Sigma-Aldrich/Merck	Germany
Protease inhibitor	11 873 580 001	Sigma-Aldrich/Merck	Germany
Protein G Dynabeads	10004D	Thermo Scientific	USA
PSN	15640–055	Gibco, Thermo Scientific	USA
Puromycin	P8833	Sigma-Aldrich/Merck	Germany
RevertAid Reverse Transcriptase kit	EP0442	Thermo Scientific	Lithuania
RNAeasy Mini Kit	74 104	Qiagen	Germany
RNAscope Fluorescent Multiplex Reagent Kit	323 110	Bio-Techne	Germany
RNase A	R4642	Sigma-Aldrich/Merck	Germany
Ribolock RNAse Inhibitor	EO0381	Thermo Scientific	USA
SB431542 (50mg)	S1067	Selleck Chemicals	USA
SSC Buffer 20x Concentrate	S6639	Merck	Germany
STEMdiff Neural Induction Medium, 250 mL	5835	STEMCELL	Canada
Stemolecule Dorsomorphin (2mg)	04–0024	Reprocell	Japan
Sucrose	4621.1	Roth	Germany
SuperFrost Plus Microscope slides	11 976 299	Thermo Scientific	Germany
SuperSignal™ West Femto Maximum Sensitivity Substrate	34 096	Thermo Scientific	USA

Table 1. Continued

Name	Catalog number	Company	Location
T3 MEGAscript kit	AM1338	Thermo Scientific	USA
T7 MEGAscript kit	AM1334	Thermo Scientific	USA
T4 RNA polymerase	18 005 025	Thermo Scientific	USA
Thiazovivin	S1459	Selleckchem	USA
Tissue freezing medium	14 020 108 926	Leica	USA
Trans-blot Turbo Transfer Pack	1 704 156	Bio-Rad	USA
TRIS hydrochloride	90 903	Roth	Germany
Triton X	3051.2	Roth	Germany
Trypsin-EDTA 0,05%	25 300 054	Gibco, Thermo Scientific	USA
Tween-20	P9416	Merck	Germany
With GoTaq® qPCR Master Mix	A6002	Promega	USA
Xho1	R0146S	New England Biolabs	USA
BaculoDirect C-Term Expression Kit	12 562 013	Invitrogen, Thermo Scientific	USA
SF900 II SFM Media	10 902 104	Gibco	USA
6x Purple Gel Loading Dye, no SDS	B7025S	NEB	USA

and adult mice were isolated from *Foxg1*$^{cre/+}$ and wild-type mice (*Foxg1*$^{+/+}$). Tissue was subsequently used for RNAseq and immunohistochemistry (IHC).

Mouse hippocampus isolation for primary neuronal culture

Hippocampi of E18.5 embryos and P0 mice were dissected from wild-type mice (C57BL/6J or CD1 with animal license X-17/03S and X-22/02B) and collected in 15 ml Hanks' Balanced Salt Solution (HBSS, Thermo Scientific, USA). The tissue was processed for plating, as previously described [20, 31]. Cells were plated at a density of 100.000 cells/cm^2 for RNA extraction or 50.000 cells/cm^2 for microscopy and electrophysiological recordings. Medium change was performed every 72 h by exchanging half of the volume of the medium with fresh NB medium with complements and AraC (1 μg/ml for the first, and 0.5 μg/ml for the second medium change, Sigma/Merck, Germany), cells were harvested at day in-vitro 7 (DIV7) (ChIPseq, RNA immunoprecipitation (RIP), RNAseq) and DIV14 (electrophysiology) based on the performed experiments.

Production of lentiviral particles and transduction

Lentiviral particles were produced and quantified in HEK293T cells with Mirus TransIT-293 Transfection Reagent (Mirus Bio LLC, Madison, WI, USA) as described before [20]. The constructs used are listed in Table 2. Constructs for lentiviral packaging were pMD2.G (Didier Trono, plasmid 12 259, Addgene, USA) and psPAX2 (Didier Trono, plasmid 12 260, Addgene, USA). Primary hippocampal cells were virally transduced at DIV1 with 1.25 IFU/cell (shRNA-mediated KD as well as rescue with *Pantr1* OE). Selection of successfully infected cells was performed 72–90 h post-infection (DIV4) by changing half of the volume of the medium with fresh NB medium containing 0.3 μg/ml Puromycin (Sigma/Merck).

IHC

Isolated mouse brains (E18.5 or P0) were fixed for 24 h, hCOs were fixed for 60 min in 4% PFA (MC1040051000, Merck, Germany). Afterwards, the tissues were incubated in 30% sucrose in DPBS (14190–094, Gibco, United Kingdom) overnight at 4°C and were subsequently embedded in tissue freezing medium (Leica, Richmond, USA). Frozen embedded tissues were cut in 14 μm sections and mounted on SuperFrost Plus Microscope slides (Thermo Scientific). Dried slides were washed twice with DPBS (14190–094, Gibco), incubated 30 min with 0.25% Triton X (Roth, Germany) in DPBS and 5 min with 0.25% Triton X in DPBS. Blocking was performed in 10% normal donkey serum (017–000-121, Jackson Immuno Research, United Kingdom), 0.1% Triton X in DPBS for 2 h at reverse transcription (RT), followed by the incubation with primary antibodies in blocking solution at 4°C overnight. After three washing steps in 0.1% Triton X in DPBS, the cover slips were incubated with secondary antibodies for 1 h at RT (dilution 1:500 in blocking solution), followed by counterstaining with DAPI (1:1000, D9542, Sigma Aldrich), three additional washing steps with DPBS and mounting in Fluorescent Mounting Medium (DAKO, S3023, Agilent, US). The antibodies used are listed in Table 6.

Immunocytochemistry

For immunocytochemistry (ICC), 50.000 cells plated on coverslips were fixed for 15 min with 4% PFA (MC1040051000, Merck). Blocking was performed in 10% normal goat serum (G6767, Sigma Aldrich) and 0.1% Triton X (Roth, Germany) in DPBS (14190–094, Gibco) for 15 min at RT, followed by the incubation with primary antibodies in blocking solution at 4°C overnight. After three washing steps in DPBS, the cover slips were incubated with secondary antibodies for 1 h at RT, followed by counterstaining with DAPI (1:1000, D9542, Sigma Aldrich) and mounting in Fluorescent Mounting Medium (DAKO). The antibodies used are listed in Table 6.

Single molecule fluorescent *in situ* hybridization

For single molecule fluorescent *in situ* hybridization (smFISH), cells (primary hippocampal neurons, NPCs) plated on 12 mm coverslips were fixed following the manufacturer's instructions for cell fixation (RNAscope *Assay for Adherent Cells*, MK50-012 TechNote_09 252 017, Bio-Techne, Wiesbaden, Germany). Isolated murine brains (E18.5 or P0) were fixed for 24 h, hCOs were fixed for 60 min in 4% PFA. Tissues were incubated in 30% sucrose in DPBS (14190–094, Gibco) overnight at 4°C, followed by embedding in tissue freezing medium (Leica). Frozen embedded tissues were cut

Table 2. List of plasmids and their shRNA sequence for lentivirus production

Plasmid carrying the coding sequence with short name (bold)	Sequence for shRNA	Comment	Producing company
pLKO.1-puro-cmv-tGFP sh_Ctrl **shCtrl**	-	used as control for *Foxg1*KD and *Pantr1*KD	MISSION® Luciferase shRNA Control SHC007V MFCD07785395
pLKO.1-puro-cmv-tGFP Sh_Foxg1_1 **shFoxg1_1**	CCG GCC TGA CGC TCA ATG GCA TCT ACT CGA GTA GAT GCC ATT GAG CGT CAG GTT TTT G	for *Foxg1*KD	SIGMA MISSION TRCN0000081746
pLKO.1-puro-cmv-tGFP Sh_Foxg1_2 **shFoxg1_2**	CCG GCT GAC GCT CAA TGG CAT CTA TCT CGA GAT AGA TGC CAT TGA GCG TCA GTT TTT G	for *Foxg1*KD	Cloned by genescript
pLKO.1-puro-cmv tGFP_Sh_Pantr1_1 **shPantr1_1**	CCG GGA ATA ACT GCC ATG GAA GGA TCT CGA GAT CCT TCC ATG GCA GTT ATT CTT TTT TG	for *Pantr1*KD	Sigma MISSION TRCN0000179216
pLKO.1-puro-cmv-tGFP_Sh_Pantr1_2 **shPantr1_2**	CCG GGG GAC AGA GTG CCT AGG TAT CTC GAG ATA CCT AGG CAC TCT GTC CCT TTT TG	for *Pantr1*KD	Cloned by genescript
pLV(Exp)-EGFP:T2A:Puro-U6 > LacZ(shRNA_2)-hPGK > mCherry **Ctrl**	-	control for rescue experiment	Cloned and packaged by Vector builder
pLV(Exp)-EGFP:T2A:Puro-U6 > FoxG1_shRNA-hPGK > mCherry **shFOXG1_Ctrl**	CCG GCC TGA CGC TCA ATG GCA TCT ACT CGA GTA GAT GCC ATT GAG CGT CAG GTT TTT G	for *Foxg1*KD in rescue experiment	Cloned and packaged by Vector builder
pLV(Exp)-EGFP:T2A:Puro-U6 > FoxG1_shRNA-hPGK>(Mouse Pantr1_201) **shFOXG1_Pantr1OE**	CCG GCC TGA CGC TCA ATG GCA TCT ACT CGA GTA GAT GCC ATT GAG CGT CAG GTT TTT G	for *Foxg1*KD and *Pantr1*OE in rescue experiment	Cloned and packaged by Vector builder

in 14 μm sections and mounted on SuperFrost Plus Microscope slides (Thermo Scientific). Probe Mm-Pantr1 (murine, 483 711, Bio-Techne) or Hs-PANTR1 (human, 1 199 961, Bio-Techne) were used following the RNAscope Fluorescent Multiplex Reagent Kit User Manual 320293-USM for detection (Bio-Techne). For smFISH in combination with ICC or IHC, the antibody incubation was performed immediately after smFISH and counterstaining with DAPI was performed at the end before mounting in Fluorescent Mounting Medium (DAKO).

Microscopy and morphometric analysis

DIV7 hippocampal neurons were stained with an antibody against Microtubule Associated Protein 2 (MAP2, 1:200, ab32454, Abcam, United Kingdom) and imaged using an Axio Imager M2 microscope equipped with an EC Plan NeoFluar 40x/0.75 M27 objective, Axiocam 506 camera, and ZEN 3.0 software. Dendrites were traced manually using the Sholl-analysis plugin for ImageJ 1.52p. Dendrite complexity was assessed by measuring the dendritic intersections in concentric circles per 10 μm from the cell soma and significance was determined using two-way ANOVA test.

For dendritic spine density analysis, biocytin-filled neurons were stained with Alexa Fluor™ 633-conjugat (1:500, S21375, Life Technologies, USA), Z-stack pictures were acquired using SP8 confocal microscope, objective HC PL APO CS2 63x/1.40 OIL, zoom 2x, and resolution 2048 × 2048. The analysis was performed by counting spines on 20 μm length dendrite, three dendrites for each neuron were quantified using LAS X 3.5.2.18963 (Leica Microsystems, Wetzlar, Germany).

For localisation and co-localisation studies, Z-stack pictures were acquired using SP8 confocal microscope, objective Zeiss HC PL APO CS2 63x/1.40 OIL, pixel size 0.361 × 0.361 μm, and analysis was performed with LAS X 3.5.2.18963 software (Leica Microsystems). For co-localisation of *Pantr1* and FOXG1 additional to the Leica system, images were taken with the 60x objective of the BC43 (Oxford Instruments, United Kingdom) and processed with Imaris 10 (Oxford Instruments).

Co-immunoprecipitation of protein and RNA

Co-immunoprecipitation (Co-IP) was performed as previously described [22]. In brief, P0 whole brain tissue, DIV7 cells, or d105 hCOs were lysed in lysis buffer (300 mM NaCl, 20 mM Tris, 1 mM EDTA, 0.5% Nonidet-40 (NP-40), pH 7.4) supplemented with protease inhibitor (Sigma-Aldrich/Merck) and incubated for 30 min on ice, triturating every 10 min 20 times. After a 10 min centrifugation at 13 000 rpm, the supernatant was collected. The samples were diluted dropwise to reach a salt concentration of 100 mM and NP-40 concentration of 0.15% using equilibration buffer (20 mM Tris, 1 mM EDTA, pH 7.4). Protein concentrations were determined with Bradford reagent (Bio-Rad, United Kingdom). Around 10% input was saved and equal amounts of protein were used for all Co-IPs. Protein G Dynabeads (10004D, Thermo Scientific) were washed with Co-IP buffer (100 mM NaCl, 20 mM Tris, 1 mM EDTA, 0.15% NP-40 pH 7.4), and incubated with

Table 3. List of primers for qPCR

Target	Forward primer	Reverse primer
murine Foxg1 [22]	AATGACTTCGCAGACCAGCA	CCGGACAGTCCTGTCGTAAA
murine Gapdh [22]	CGGCCGCATCTTCTTGTG	TGACCAGGCGCCCAATAC
murine Pantr1	CGGGACTGTAAGGCGGATAA	GTCCCTCTCCCTCGATGTCA
human ACTIN B [61]	CTGGAACGGTGAAGGTGACA	AAGGGACTTCCTGTAACAATGCA
human FOXG1 [62]	CCCTCCCATTTCTGTACGTTT	CTGGCGGCTCTTAGAGAT

Co-IP antibodies at 4°C overnight. The following antibodies were used: anti-FOXG1 (61 211, Active Motif, USA; or SAB2102981, Sigma-Aldrich for mass spectrometry) and IgG (C15410206 or C15400001, Diagenode, Belgium). Antibody-coupled beads were washed once with Co-IP buffer before Co-IP. Cell lysates were precleared with Protein G Dynabeads for 1 h at 4°C, subsequently transferred to antibody-coupled beads, and incubated overnight at 4°C in rotation. If the aim was to investigate binding and complex forming in absence of RNA, RNase A (1:400, R4642, stock concentration 20–40 mg/ml, Sigma-Aldrich/Merck) was added to this overnight step. Antibody-coupled beads were washed three times with Co-IP buffer. Depending on downstream analysis they were either resuspended in 1x Laemmli sample buffer (protein detection by immunoblotting) or in RLT buffer of the RNA isolation kit (RNA detection by native RIP). Protein–antibody complexes were eluted by incubating the beads at 70°C for 10 min at 550 rpm. Around 10% input and the complete Co-IP sample were used for immunoblotting (IB). The samples were used for IB or mass spectrometry (MS). MS data were processed by the Proteomics core facility (Proteomics Platform – Core Facility (ProtCF), Institute of Surgical Pathology and Institute of Molecular Medicine at the Medical Faculty of the University of Freiburg, Germany). Here, proteins bound to beads were resuspended in lysis buffer (5% SDS, 50 mM triethyl ammonium bicarbonate (TEAB), pH 7.5) and incubated at 95°C for 10 min for elution. Samples were centrifuged at 13 000 rpm for 8 min, and the supernatant further processed and measured as described [32].

IB

Co-IP samples were loaded onto 10% sodium dodecyl sulphate (SDS)-polyacrylamide gels and electrophoresed at 120 V for 1.5 h in Tris-Glycine running buffer. Subsequently, proteins were transferred onto PVDF membranes (Trans-blot Turbo Transfer Pack, Bio-Rad, USA) using the Trans-blot Turbo Transfer System (Bio-Rad), following the manufacturer's instructions. Afterwards, the membranes were blocked with 5% bovine serum albumin (BSA, 8076.4, Roth) in Tris-buffered saline (TBS) for 1 h. For IB, the following antibodies were used: anti-FOXG1 (61 211, Active Motif), anti-NEUROD1 (ab109224, Abcam), anti-DDX5 (9877, Cell Signaling, USA), anti-PURB (ab130999, Abcam) diluted in 5% BSA in TBST (TBS with 0.1% Tween-20 (Merck)). After three washes with TBST, the membranes were incubated with HRP-linked rabbit IgG (diluted 1:10 000 in 5% BSA in TBST, Cell Signaling, 7074) or Tidyblot (diluted 1:5000 in 5% BSA in TBST, Biorad), for 1 h. Following two washes with TBST and two with TBS, the membranes were developed using SuperSignal™ West Femto Maximum Sensitivity Substrate (diluted 1:2–1:4, Thermo Scientific) and imaged with the LAS ImageQuant System (GE Healthcare, USA).

RNA isolation, RT, and qPCR analysis

RNA was isolated from tissue, organoids, cell samples, or co-IP beads directly after harvesting or after storage at −80°C with the RNAeasy Mini Kit (74 104, Qiagen, Germany) including an on-column DNAse digestion (79 254, Qiagen). The isolated RNA was either used for further RNAseq or for qPCR analysis. For qPCR analysis, we harvested 1 Mio cells or one organoid in RLT buffer (74 104, Qiagen). Around 1 µg of total RNA was used to synthesise cDNA with the RevertAid Reverse Transcriptase kit (EP0442, Thermo Scientific) following the manufacturer's protocol with a total volume of 20 µl. Subsequently, 5 µl of 1:50 diluted cDNA was used for a qPCR with GoTaq® qPCR Master Mix (A6002, Promega, WI, USA) following the manufacturer's protocol with three technical replicates. Primers (Sigma/Merck) are listed in Table 3. For qPCR after co-IP, half of the total RNA of the co-IP samples or input sample was used to synthesise cDNA with the RevertAid Reverse Transcriptase kit (EP0442, Thermo Scientific) following the manufacturer's protocol with a total volume of 20 µl. Subsequently, 5 µl of 1:5 diluted cDNA was used for a qPCR with GoTaq® qPCR Master Mix (A6002, Promega) following the manufacturer's protocol with three technical replicates. The Ct values were used to calculate the percentage of RNA left after co-IP compared to the cell lysate (input). All other analyses were performed as described before [20]. Data are presented as mean ± SEM. *P*-values were calculated using unpaired, two tailed Student's t-test, one-way ANOVA, or non-parametric tests: $*P < 0.05$, $**P < 0.01$, $***P < 0.001$ with GraphPad Prism 6.

Single cell (sc)RNAseq library preparation

Two organoids of each line were collected at day 105, and single cells were obtained according to the protocol of the Papain Dissociation System (Worthington, Lakewood, USA), with centrifugation steps carried out at 4°C. Library preparation was performed with the 10x Genomics kit according to the manufacturer's instructions (Chromium Next GEM Single Cell 3′ Reagent Kits v3.1, 10X Genomics, CA, USA).

Bulk RNA-sequencing and RIPseq

Total RNA extracted from mouse hippocampi, cortex, or DIV7 primary hippocampal neurons were used for RNAseq. Total RNA extract of FOXG1- and IgG-co-IP respectively were used for RIPseq. The cDNA libraries were constructed using TruSeq total RNA sample preparation kit (Illumina, USA), following the manufacturer's instructions and sequenced on Illumina HiSeq 3000 as paired-end 101 bp reads. For RNAseq, the procedure included depletion of rRNA prior to double-stranded cDNA synthesis and library preparation. Each replicate (n) came from independent cell cultures of different litters, respectively, from independent mice.

Table 4. List of primers for ChIP- and ChIRP-qPCR

Target	Forward primer	Reverse primer
human PANTR1 promoter	CTTCTACGACGCTCTGCCTAA	TACAAGGAAGTCGAGCACCAG
human PANTR1 exon	CCGAGTTGGGTTAGTTCATTGG	GGAACCTCAGCGAACCAAGAA
mouse Slc8a1	TTGGTTTCTCTGCCTGACCTG	CGCATTATTTGACACCGAGGC
mouse Cdkn1a	GTTGTCCTCGCCCTCATCTAT	CGGACACTCGAGAGCAAAGAA
mouse Sox5	TCCCGGGACTTGAACAAACTC	GTGAACCGCAGCGTTTTAACT
mouse Pantr1	ACATCTCCACCTCCACCAATG	TTGCTGAAGGTTGGGGTTGAT
mouse Tmem2	CGTAGGTTGCCGCTGAATTC	TCTACTCAGGTGTCTACGCGA
mouse St18	GTTCCCAGAGTTTCAGGCAGA	ATATGGCAGACAGGAACAGGC
mouse Sephs1	ATTCAGGCGACGCTTAAGGG	CCGCTATTCCCCTTTAAGCCT

ChIPseq and ChIP-qPCR

For FOXG1-ChIPseq analysis, wildtype or virally transduced primary hippocampal neurons were fixed and collected as previously described [22], following the instructions of the servicing company (Active Motif). For FOXG1-ChIPseq analyses after *Pantr1*KD, primary hippocampal neurons transduced with lentiviral shPantr1_1 constructs or control constructs were fixed on DIV7. The FOXG1-ChIPseq of cortical organoids was performed after their fixation using the same protocol as for cells.

A custom Illumina library type on an automated system (Apollo 342, Wafergen Biosystems/Takara) was used to generate ChIPseq libraries, which were subsequently sequenced on Illumina NovaSeq 6000 as single-end 75 bp reads (Active Motif). Antibodies used for the immunoprecipitation were either anti-FOXG1 (61 211, Active Motif) for murine samples or anti-FOXG1 (ab18259, Abcam) for human samples.

For ChIP-qPCR, d105 hCOs were crosslinked with 1% formaldehyde, lysed, and chromatin was sheared to 200–500 bp by sonication. Around 5–10% input was collected prior to ChIP, which was performed using anti-FOXG1 antibody (rabbit, 61 212, Active Motif) or control rabbit IgG (C15410206, Diagenode) in combination with Protein G Dynabeads (10003D, Invitrogen). Immunoprecipitated DNA was reverse crosslinked and purified using the MinElute Reaction Cleanup Kit (28 204, Qiagen), then quantified by qPCR with locus-specific primers (Table 4), and displayed normalized to input and IgG controls.

RNA pulldown of adult hippocampus protein extracts

Pantr1 lincRNA was cloned into pBluescript plasmid such that the sense strand was in frame with T7 promoter and antisense strand with T3. *Pantr1* RNA sense strand was synthesised *in vitro* using linear pBluescript-Pantr1 plasmid (linearized using Xho1 (New England Biolabs, USA)) and T7 RNA polymerase (T7 MEGAscript kit, Thermo Scientific) as per the manufacturer's protocol. Similarly, *Pantr1* antisense strand was synthesised by using Not1 (New England Biolabs) digested linear pBluescript-Pantr1 plasmid and T4 RNA polymerase (T3 MEGAscript kit, Thermo Scientific). Next, 10 µg of *Pantr1* sense RNA were used to label the 3′ end using Pierce™ RNA 3′ End Desthiobiotinylation Kit (Thermo Scientific). After labelling, *Pantr1* sense RNA was purified to remove the unincorporated labelled nucleotides, and RNA pull down was performed using Pierce™ Magnetic RNA-Protein Pull-Down Kit (Thermo Scientific) according to the instructions. Protein extracted from 6-week old NMRI mouse hippocampus were used for the RNA pull down assay (with animal license X-14/04H). RNA pulldown samples ($n = 3$) were collected and subjected to LC-MS/MS to identify the proteins interactome of *Pantr1* lincRNA.

Recombinant FOXG1 protein expression

Recombinant FOXG1 protein was expressed using the BaculoDirect C-Term Expression Kit (12 562 013, Invitrogen, USA) according to the manufacturer's instructions. The mouse FOXG1 coding sequence was initially cloned into the pENTR vector and subsequently transferred into the baculoviral destination vector via Gateway recombination. Recombinant bacmid DNA was used to transfect *Spodoptera frugiperda* (Sf9) cells. Following viral amplification, high-titer P3 virus was used to infect 300 ml cultures of Sf9 cells for large-scale protein expression. Infected cells were harvested 72 h post-infection and lysed using lysis buffer, followed by ultracentrifugation to clarify the lysate. FOXG1 protein was purified using Ni-NTA beads (30 210, Qiagen), with elution performed via an imidazole gradient (100–500 mM). Eluted fractions were analysed by SDS-PAGE and IB, and those containing high levels of FOXG1 were pooled. The protein was then concentrated and partially desalted using 10 kDa molecular weight cutoff centrifugal filters (Vivaspin, Sartorius, Germany), followed by further purification via immunoprecipitation using anti-FOXG1 antibody (61 211, Active Motif). Finally, the buffer was exchanged to the binding buffer (20 mM Tris-HCl, 50 mM NaCl, 1 mM EDTA) using the same centrifugal filters, and protease inhibitor cocktail was added (cOmplete, Sigma-Aldrich).

Chromatin isolation by RNA purification

Chromatin isolation by RNA purification (ChIRP) was performed using biotinylated antisense DNA probes targeting the RNA of interest, following a previously published protocol with minor modifications [33]. For one ChIRP experiment, mouse cortices from three P0 mice were pooled and snap-frozen. The tissue was thawed, dissociated in phosphate-buffered saline (PBS), crosslinked with 1% glutaraldehyde for 10 min at room temperature to preserve RNA–chromatin interactions, and subsequently quenched with 125 mM glycine for 5 min. After lysis, chromatin was sonicated for 60 min using Covaris E220 (USA). Around 5–10% input was collected prior to hybridization. Approximately 100 pmol of a pool of 20–25 biotinylated antisense DNA probes (20-mers, spaced every ∼100 nt across the full-length transcript) (Table 5) were hybridized to the chromatin lysate overnight at 37°C with rotation. Hybridised complexes were captured using Pierce Streptavidin Magnetic Beads (88 816, Thermo Scientific) for 2 h at 37°C with rotation. After stringent washes, DNA was

Table 5. List of Pantr1 ChIRP probes

Name	Sequence
Pantr1_ChIRP_probe_1	CGTGGCTTCGTTGACCGG[BtnTg]
Pantr1_ChIRP_probe_2	CCCAGGGCAATATTCACT[BtnTg]
Pantr1_ChIRP_probe_3	CAAAGTTAGGAACGGCCA[BtnTg]
Pantr1_ChIRP_probe_4	CTTATCCGCCTTACAGTC[BtnTg]
Pantr1_ChIRP_probe_5	CAGCACTTTCTGTTGGGG[BtnTg]
Pantr1_ChIRP_probe_6	CCACATGGATGATGTCCA[BtnTg]

eluted using 100 mM $NaHCO_3$ and 1% SDS. Crosslinks were reversed by incubating with RNase at 37 °C for 30 min, followed by Proteinase K treatment at 55 °C for 2 h. DNA was purified using the MinElute Reaction Cleanup Kit (28 206, Qiagen) and analysed by qPCR using locus-specific primers (Table 4). Results were normalised as percentage of input.

RNA-protein electrophoretic mobility shift assay

RNA-protein electrophoretic mobility shift assay (EMSAs) were performed to assess direct binding of FOXG1 to *Pantr1* RNA. *In vitro* transcribed *Pantr1* RNA was incubated with increasing concentrations of recombinant FOXG1 protein in binding buffer (20 mM Tris-HCl, 50 mM NaCl, 1 mM EDTA, 5% glycerol) at room temperature for 30 min. Samples were loaded with 5x Purple Loading Dye (NEB, no SDS) and resolved on 5% native PAGE gels in 1x TAE buffer. RNA was visualised by post-staining with 3x GelRed (Biotium, USA). Shifted RNA–protein complexes appeared as slower-migrating bands compared to free RNA.

DNA:DNA:RNA hybridisation EMSA

To assess triplex formation, a double-stranded DNA fragment corresponding to the *Pantr1* target site was amplified by PCR from mouse genomic DNA and purified using the MinElute Reaction Cleanup Kit (28 206, Qiagen). The DNA was incubated with *in vitro* transcribed *Pantr1* RNA in triplex binding buffer (10 mM Tris-HCl, 50 mM NaCl, 10 mM $MgCl_2$) at 60°C for 1 h. Complexes were resolved on 2% agarose gels in 1x TAE buffer. Triplex formation was inferred from reduced electrophoretic mobility relative to free DNA.

Bioinformatics

Single cell RNA sequencing analysis

Reads from single cell (sc)RNAseq were aligned to the GRCh38 human reference genome, and the cell-by-gene count matrices were produced using the *RNA STARSolo* on the Galaxy Platform. Data were analysed using the *Seurat R package v.4.3.0* with *R v.4.2.2*. The following parameters were used for filtering cells: cut_nUMI ← 500; cut_nGene ← 250; max_nGene ← 8500; cut_log10GenesPerUMI ← 0.80; cut_mito.Ratio ← 0.2; cut_ribo.Ratio ← 0.2.

The expression values were normalised using the *'SCTransform v2'* function. Subsequently, Principal Component Analysis (PCA) was applied to highly variable genes identified by the '*FindVariableGenes*' function, retaining the top 40 principal components (PC) based on Seurat's Elbow Plots and determination of percent variation associated with each PC. Clustering was executed on the PCA-reduced data utilising the '*FindNeighbors*' and '*FindClusters*' functions, with a resolution set at 0.4. Uniform Manifold Approximation and Projection (UMAP) was employed for dimensionality reduction, providing a visual representation of the data. For cell-type annotation, differential expression analysis was conducted between clusters via the '*FindAllMarkers*' function, considering genes with a log-fold change greater than 0.1 and an adjusted *P*-value less than 0.05 as differentially expressed. FOXG1 and *PANTR1* expression levels were plotted using *VlnPlot* and *FeaturePlot* functions within the Seurat package. Cell-type proportions were calculated using *scProportionTest* tool with default settings [34].

Bulk RNA-, ChIP-, RIP sequencing analysis

The Galaxy platform as well as R based analysis were used to analyse the RNAseq, FOXG1 ChIPseq and RIPseq data. Mapping was performed on mouse genome build mm10 (GRCm38) or human genome build hg38 depending on organism.

Quality control, trimming, mapping of the RNAseq fastq files, and generation of gene-level counts was done on the Galaxy platform [35]. Differential expression analysis of DIV7 hippocampal neurons (Fig. 5B) was done using *DESeq2* (1.34.0) on *R* (4.2.0) on the count matrix output from *featurecounts* [36]. Gene ontology (GO)-term enrichment analyses were done using *clusterProfiler* (4.2.2) [37]. Visualisations of volcano plots and heatmaps were done using *EnhancedVolcano* (1.12.0) and *pheatmap* (1.0.12) packages, respectively [38–40].

Differential expression analysis for RNAseq of the adult and E18.5 hippocampus sample (Fig. 3C) was done using DESeq2 (v. 1.22.1) [36] on count matrices output from snakePipes (featureCounts, v. 1.6.4) [41]. A linear model controlling for batch effects (e.g. ∼batch + treatment or ∼ batch + condition) was used and apeglm log2(fold change) shrinkage was applied.

RIPseq fastq files were processed on the Galaxy platform. Trimmed and quality filtered reads were aligned to mm10 genome assembly using *RNAStar* (2.7.10b). FOXG1-coIP reads were normalized to IgG-coIP reads using *bamcompare* (v. 3.5.4) and the average calculated using *bigwigAverage* (v. 3.5.4). Differentially immunoprecipitated RNA was calculated using *DESeq2* (v. 2.11.4.0.8) after generating count matrices (featureCounts, v. 2.0.3).

FOXG1 ChIPseq quality controls were performed on the galaxy server (usegalaxy.eu). The sequences were mapped against mm10 with Bowtie and Peaks were called using MACS callpeak. The coverage was calculated followed the analyses as described previously [22].

GO enrichment and differential GO-term analyses were performed using *clusterProfiler* (v. 4.2.2) [37].

Motif enrichment and differential motif enrichment analyses of the ChIPseq dataset were done using *gimmemotifs* on Python [42].

Visualisations were done in Galaxy, R (v. 4.1) and Python (v. 3.6). Heatmaps were plotted using *heatmap2* (Galaxy Version 3.0.1), genome tracks using *pyGenomeTracks* (Galaxy Version 3.6), venn diagrams using *ggVenn* (Linlin Yan (2021), ggvenn: Draw Venn Diagram by "ggplot2". R package version 0.1.9) and *VennDiagram* (Hanbo Chen, VennDiagram: Generate High-Resolution Venn and Euler Plots. R package version 1.7.3. (2022) packages, volcano plots using *EnhancedVolcano* (BioConductor, v. 3.13) (B. K. Lewis M Rana S., EnhancedVolcano: Publication-ready volcano plots with enhanced colouring and labeling. R package version 1.14.0, (2022)), violin plots using *ggplot2* (v. 3.3.5) [43].

Table 6. List of antibodies

Name	Usage and dilution	Source
FOXG1	IHC, 1:500	Abcam, ab196868, United Kingdom
FOXG1	IB, 1:1000, coIP, RIP	Active Motif, 61 211, USA
FOXG1	coIP	Sigma-Aldrich, SAB2102981, Germany
DDX5	IB, 1:1000	Cell Signaling, 9877, USA
NEUROD1	IB, 1:1000	Abcam, ab109224, United Kingdom
PURB	IB, 1:1000	Abcam, ab130999, United Kingdom
GFAP	IHC, 1:500	Life Technologies, 13–0300, USA
MAP2	ICC, 1:200	Abcam, ab32454, United Kingdom
NeuN	IHC, 1:150	Abcam, ab177487, United Kingdom
PAX6	IHC, 1:150	BioLegend, 901 301, USA
TBR1	IHC, 1:200	Abcam, ab31940, United Kingdom
TBR2	IHC, 1:200	Invitrogen, 14–4875-82, USA
TUJ-1 (TUBB3)	IHC, 1:200	BioLegend, MMS-435P-100, USA
vGLUT1	IHC, 1:500	Synaptic Systems, 135 303, Germany
vGLUT2	IHC, 1:500	Abcam, ab79157, United Kingdom
anti Mouse-Alexa488	ICC, IHC 1:500	Dianova (715–545-151), Germany
anti Mouse-Alexa594	ICC, IHC 1:500	Dianova (715–585-151), Germany
anti Rabbit-Alexa488	ICC, IHC 1:500	Dianova (711–545-152), Germany
anti Rabbit-Alexa594	ICC, IHC 1:500	Dianova (711–585-152), Germany
anti Rat-Alexa488	ICH, 1:500	ThermoFisher, A21208, USA
Streptavidin-Alexa-633	ICC, 1:500	Life Technologies, S21375, USA
Tidyblot	IB, 1:5000	Bio-Rad, Tidyblot STAR209P, USA
Anti-rabbit HRP-linked IgG	IB, 1:10 000	Cell Signalling, 7074

Pantr1–Triplex-forming potential analysis

The potential of *Pantr1* to form RNA–DNA triplexes was assessed using the Triplex Domain Finder (TDF) tool from the RGT-Regulatory Genomics Toolbox [44]. This tool predicts specific regions within a l(i)ncRNA likely to form DNA-binding domains (DBDs) that can interact with defined target DNA regions. We used the *Pantr1* sequence from the NCBI mm10 genome (Gene ID: 66 297) as input RNA and assessed its binding potential against two sets of target DNA regions: (1) differentially bound FOXG1 regions upon *Pantr1* knockdown (*Pantr1*KD) and (2) promoter regions from the mm10 genome. The analysis was performed using the default parameters provided by the tool.

Prediction of Direct FOXG1–Pantr1 binding propensity

To evaluate the potential for direct interaction between FOXG1 and *Pantr1*, we used the catRAPID omics v2.1 web server (http://service.tartaglialab.com/page/catrapid_omics2_group). The analysis was performed using the 'custom protein set vs custom transcript set' mode. The NCBI-derived *Pantr1* transcript sequences from the mm10 and hg38 genomes, along with the corresponding FOXG1 protein sequences for mouse and human obtained from UniProt (accession numbers: Q60987 for mouse, P55316 for human), were submitted to the web server. Default settings were used for the prediction.

Analysis of FOXG1-co-immunoprecipitated proteins after Co-IP-MS

Raw data were analysed with MaxQuant (v 2.1.4.0) with the built-in Andromeda peptide search engine [45] allowing two missed cleavage sites, no variable modifications, and carbamidomethylation of cysteines as fixed modification. The match between runs option was selected. The Human-EBI-reference database was downloaded from https://www.ebi.ac.uk/ on July 22nd 2020. For label-free quantification, the MaxLFQ algorithm was applied using the standard settings. Only unique peptides were used for quantification.

Statistics

GraphPad Prism software (version 6) was used for statistical analyses. Depending on the experimental design, two-sided unpaired Student's t-test or two-sided one-way ANOVA followed by Tukey multiple comparisons, or Kruskal–Wallis test were used for the analyses of qPCR experiments. RNAseq and RIPseq counted features were statistically analysed using the Deseq2 tool [36] provided by the Galaxy platform [40]. Statistics in scRNAseq and pseudobulk RNAseq analysis of the organoids are described in the bioinformatics section in the supplement. Statistical significance in ChIPseq data were analysed using the *Diffbind* tool [46] on the Galaxy platform. Electrophysiological recordings were tested using Mann–Whitney test, and Sholl analysis was tested with two-sided two-way ANOVA followed by Sidak's multiple comparison test.

Results

iPSC-derived human brain organoids as model for FOXG1-syndrome

To explore the molecular underpinnings of FOXG1-syndrome in human model systems, we used human patient derived iPSC carrying one allele with a full deletion of FOXG1 (FOXG1del) and one hotspot frameshift mutation, c.460dupG (FOXG1c460). We generated hCO, which we cultured for 105 days (d). hCO expressed marker genes for progenitors, glutamatergic, and GABAergic neuron populations, including FOXG1, in the HD (Supplementary Fig. S1A and B). FOXG1del and FOXG1c460 derived hCO expressed less FOXG1 protein and significantly less *FOXG1* transcripts (Supplementary Fig. S1B and C). To characterise the hCO in detail at the transcriptional level, we performed scRNAseq on 11 258 cells from the HD control, 9292 cells from FOXG1del, and 9374 from FOXG1c460 organoids. UMAP representation of cell clusters retrieved stem and progenitor cells, as well as diverse stages and subtypes of excitatory and inhibitory neurons (Fig. 1A). By plotting *FOXG1* expression

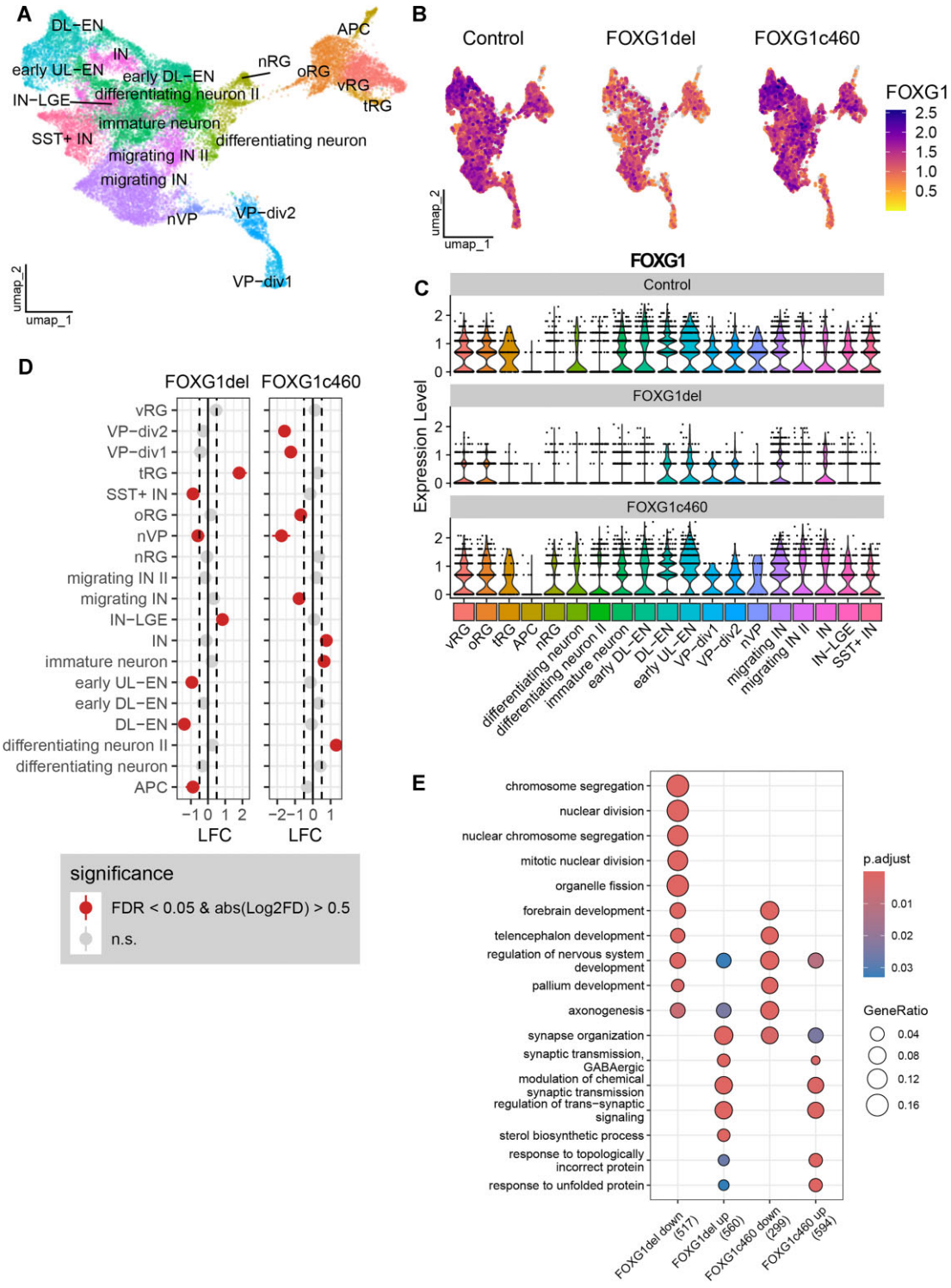

Figure 1. iPSC-derived hCO model FOXG1-syndrome. (**A**) UMAP plot, colour-coded and annotated by cell type, depicting the d105 cerebral organoids (hCO, brain organoids) obtained from a HD and FOXG1-syndrome patients featuring a heterozygous deletion of *FOXG1* (FOXG1del), and *FOXG1c460.dupG* (FOXG1c460) mutation, $n = 2$. Number of cells: Control = 11 258, FOXG1del = 9292, FOXG1c460 = 9374. Abbreviations: APC: Astrocyte progenitor cells, DL-EN: Deep layer excitatory neuron, IN: Interneuron, IN-LGE: interneurons of the lateral ganglionic eminence, nIP: neuronal intermediate progenitor, nRG: neuronal radial glia (RG), nVP: neurogenic ventral progenitor, oRG: outer RG, SST + IN: Somatostatin-positive interneurons, tRG: truncated RG, UL-EN: Upper layer excitatory neuron, VP-div: Ventral progenitor-dividing, vRG: ventricular RG. (**B**) UMAPs of healthy, FOXG1del, and FOXG1c460 organoids coloured by expression level of *FOXG1* (low: grey; high: purple to yellow). (**C**) Violin plots of cell-type specific expression distribution of *FOXG1*. *FOXG1* expression was reduced across all cell populations upon FOXG1 deletion, whereas the FOXG1c460 mutation led to either increased or decreased expression depending on the cell type. (**D**) Dotplot of the ratio of cell type proportions of FOXG1del (left) and FOXG1c460 (right) organoids compared to the control organoids. Shown is the log2(fold change) (LFC). A significance threshold of false discovery rate (FDR) < 0.05 and a LFC < -0.5 or > 0.5 was applied. Significant values are marked in red. (**E**) GO-term enrichment analysis of pseudobulk DEGs in FOXG1del and FOXG1c460 organoids, separated into downregulated (down) and upregulated (up) genes relative to HD hCOs. Shown are the top five enriched GO terms with a FDR < 0.05.

levels, we observed broad expression of *FOXG1* and reduced levels of it upon *FOXG1* mutation compared to the HD (Fig. 1B). Cluster-wise comparison of expression levels of *FOXG1* in HD and both FOXG1-mutated hCO revealed that *FOXG1* was transcribed by all cells but in different levels (Fig. 1C). Upon deletion of one *FOXG1* allele, all cell clusters showed reduced *FOXG1* transcription, while upon the c460 frameshift mutation, *FOXG1* expression levels varied across cell types. While some clusters such as outer radial glia (oRG), early deep-layer excitatory neurons (early DL-EN), and immature neurons exhibited moderately increased *FOXG1* expression compared to HD, others, including ventricular radial glia (vRG), astrocyte progenitor cells (APC), and neurogenic ventral progenitors (nVP), showed decreased expression, indicating a non-uniform regulatory effect of the mutation across neurodevelopmental cell lineages (Fig. 1C). We observed significant changes in cell proportions for some specific clusters upon *FOXG1* deletion, including APC, truncated radial glia (tRG), three interneuron (IN) populations (somatostatin expressing (SST+)-IN, nVP, IN of the lateral ganglionic eminence (LGE)), and two excitatory neuron (EN) populations (DL-EN, early upper layer (UL)-EN) (Fig. 1D). FOXG1c460 organoids also exhibited changes in cell-type proportions, albeit varying from FOXG1del organoids. Both dividing (VP-div) and nVP populations decreased in proportion, while immature and differentiating neuron populations, and IN increased. Also, many populations that significantly decreased in FOXG1del did not change significantly in FOXG1c460 organoids. These differences indicate that both genotypes disrupt the balance of cell types in distinct ways.

Functional GO-terms of pseudobulk scRNAseq analysis associated lower expressed genes in FOXG1del hCO to processes including regulation of neurogenesis and neuron fate commitment, whereas higher expressed genes correlated to processes including nerve development and neuron apoptosis. FOXG1c460-associated transcriptional changes also converged on key neurodevelopmental processes. Genes with lower expression in FOXG1c460 were enriched for terms related to synaptic signalling and neuronal differentiation. As in FOXG1del, GO-terms associated with telencephalon and forebrain development, axonogenesis, and synapse organisation appeared in both up- and downregulated gene sets, indicating a disruption of region-specific neuronal maturation programs (Fig. 1E).

In mice, FOXG1 functions at the chromatin level [22]. We therefore performed ChIPseq using FOXG1 antibody at d105 of the HD hCO. FOXG1 bound transcription start sites (TSS) distributed similar to mouse [47], i.e. concentrated around the TSS (cluster 3, Fig. 2A) but also dispersed (cluster 1, Fig. 2A). Similar to what has been described for the mouse hippocampus, FOXG1 bound mainly intronic (first intron: 10.84 %, other introns: 28.73 %) and intergenic regions (especially distal intergenic: 25.87 %) as well as promoters (predominantly near promotor $\leq$ 1 kb: 24.36 %) (Fig. 2B). Genes bound by FOXG1 in HD conditions classified as genes involved in axonogenesis and forebrain and telencephalon development (cluster 1) as well as ncRNA processing and RNA splicing (cluster 3) in enriched functional GO-terms (Fig. 2C). Intersection of differentially expressed and FOXG1 bound regions revealed 266 potentially direct FOXG1 target genes in hCO that changed expression upon deletion of one *FOXG1* allele, the condition modelling best our mouse data (Fig. 2D). Functional GO-terms associated the differentially expressed genes (DEGs) in FOXG1del hCO to processes like forebrain development, axonogenesis and axon guidance (Fig. 2E). Together, the characterisation of HD and FOXG1del hCO indicated similarities to the mouse model at the chromatin and transcriptional level. We concluded that parallel analysis of human and mouse multiomic data might help identifying and functionally assessing regulative factors of FOXG1.

FOXG1 binds to gene loci encoding for l(i)ncRNAs in mouse and human

To extend the multi-omics comparison between mouse and human FOXG1 functions to the protein level, we determined the FOXG1 interactome from HD hCO. Strikingly, both mouse and human interactomes enriched for RNA binding proteins (RBPs) (Fig. 3A), implying both transcriptional and post-transcriptional regulations through FOXG1 in both species. We therefore categorized first the RNA species targeted at the transcriptional level by FOXG1 using the ChIPseq experiments of mouse adult hippocampus (*in vivo*) and primary hippocampal neurons (*in vitro*) (Fig. 3B), as well as hCO (Fig. 3C). In mouse, protein-coding RNAs comprised the largest fraction, compared to non-coding RNAs, of which 520 genomic loci associated with l(i)ncRNAs *in vivo*, and 788 *in vitro*, with 488 shared among both datasets (Fig. 3D). To investigate whether l(i)ncRNA expression was affected upon loss of FOXG1, we explored $Foxg1^{cre/+}$ adult hippocampus, the developing $Foxg1^{cre/+}$ E18.5 hippocampus [22], and the $Foxg1^{cre/cre}$ E13.5 cerebral cortex RNAseq datasets. We identified altered expression of 8 l(i)ncRNAs in adult hippocampal tissue, 17 in the developing hippocampus, and 193 in the cerebral cortex upon *Foxg1* mutation, using a threshold of adjusted *P*-value (padj) < 0.05 (Fig. 3E, F). L(i)ncRNAs common to all mouse transcriptome datasets were *Pantr1* and *Firre*, of which only *Pantr1* occurred in the shared targets of *in vivo* and *in vitro* FOXG1 ChIP peaks (Fig. 3D). In support of these findings, we validated decreased levels of *Pantr1* in the $Foxg1^{cre/+}$ adult hippocampus using RT-qPCR (Supplementary Fig. S2A).

In hCO, 2694 genomic loci classified as l(i)ncRNAs bound by FOXG1, comprising the largest fraction after mRNAs (Fig. 3C). The high representation of l(i)ncRNAs in the human data set let us to explore further potential roles of them in FOXG1-syndrome. Pseudobulk scRNAseq analysis comparing FOXG1del to HD of the hCO transcriptomes revealed 85 l(i)ncRNAs among the DEGs (Fig. 3G). 25 l(i)ncRNA were common in both ChIPseq and pseudobulk scRNAseq datasets. The only common l(i)ncRNA between mouse and human datasets, analysed in the same manner, was *PANTR1*. ChIPseq tracks for both human and mouse *PANTR1* loci revealed multiple potential FOXG1 binding sites, a subset of which showed enrichment of FOXG1 (Fig. 3H). The potential binding site in hCO was assigned to cluster 1 (Fig. 2A). FOXG1 ChIP-qPCR confirmed its binding to the *PANTR1* promoter and exon (Supplementary Fig. S2B). RT-qPCR confirmed altered *PANTR1* levels in FOXG1del and FOXG1c460, but with high variability and opposing direction (Supplementary Fig. S2C). These data together rendered *PANTR1* as direct target gene of FOXG1.

We therefore plotted *PANTR1* expression levels in hCO in single cell resolution and observed mainly reduced levels of *PANTR1* in FOXG1del and FOXG1c460 compared to the HD (Fig. 3I). Cluster-wise comparison of expression levels of *PANTR1* in HD, FOXG1del, and FOXG1c460 hCO revealed

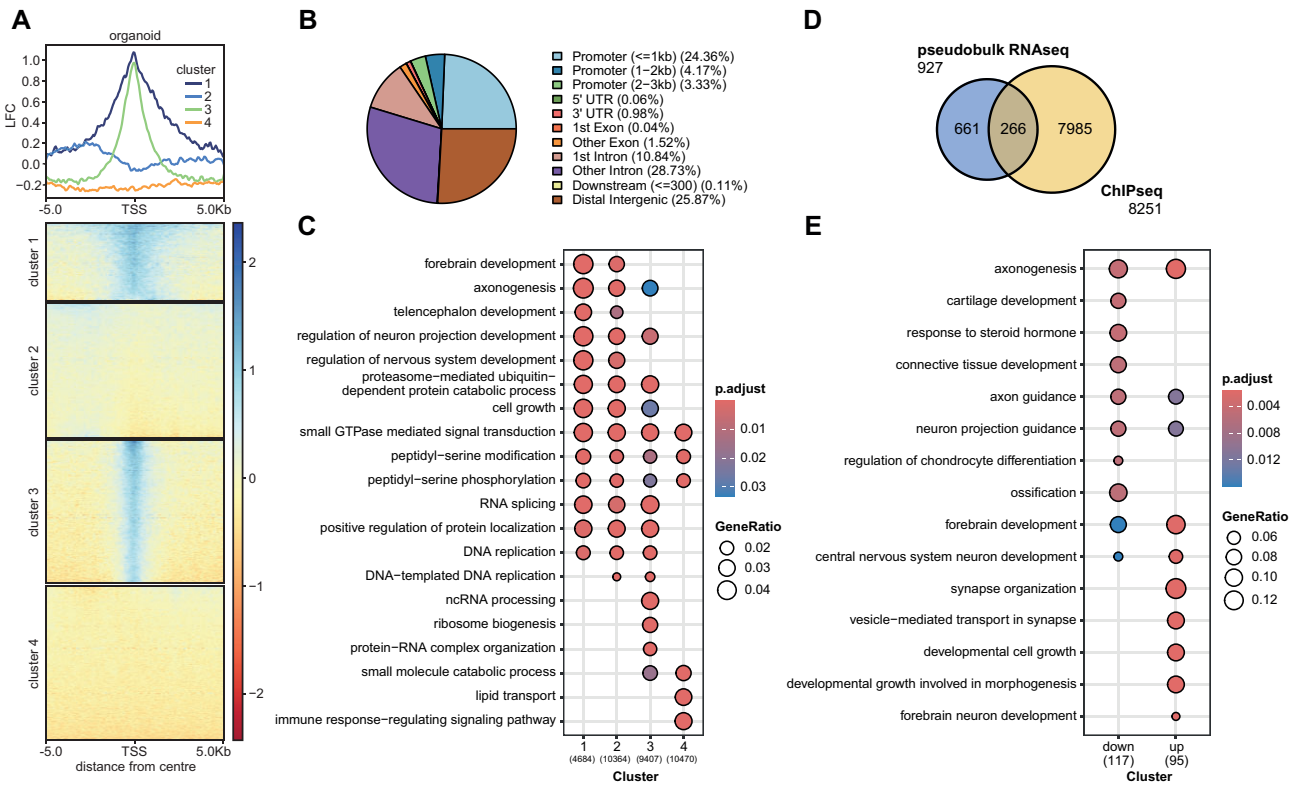

Figure 2. FOXG1 bound gene loci in hCO encode for genes correlating with neural development and RNA processing. (**A**) Heatmap of differently bound regions (DBRs) of FOXG1, 5 Kb up-/downstream of FOXG1 peak summits in d105 heathy donor hCO. The metaprofiles (top) show the mean log2(fold change) (LFC) of 4 k means clustered regions compared to the input. (**B**) Genome-wide distribution of bound regions of FOXG1 in d105 HD hCO in percentage for near and far promotor regions, 5′UTR, intronic and exonic as well as distal intergenic regions. (**C**) GO-term enrichment analysis of genes located near to the peaks in the ChIPseq data split according to the clustering in Fig. 2A. Given are the top enriched GO terms with a FDR < 0.05. (**D**) Venn diagram of FOXG1 enriched peaks and pseudobulk DEGs upon deletion of one FOXG1 allele (FOXG1del) in d105 hCO. (**E**) GO-term enrichment analysis of common genes in the ChIPseq and pseudobulk RNAseq data sets split according to DEGs with either increased or decreased expression compared to HD d105 hCO. Given are the top enriched GO-terms with a FDR < 0.05.

that *PANTR1* expression was more cell-type restricted compared to *FOXG1* expression (Figs 3J and 1C). *PANTR1* was mainly expressed by distinct RG cells and developing IN. Accordingly, in FOXG1del or FOXG1c460, *PANTR1* expression reduced in RG and IN. Interestingly, depending on the *FOXG1* mutation individual cell clusters seemingly showed increased expression of *PANTR1*, namely early UL-EN in FOXG1del, and APCs in FOXG1c460 (Fig. 3J). We investigated whether changes in cell proportions upon *FOXG1* mutation were associated with altered *PANTR1* expression (Fig. 1D). While *PANTR1* was highly expressed in specific clusters such as DL-EN, early UL-EN, and VP populations, its expression remained relatively stable across genotypes and did not correlate with changes in cluster abundance. These findings indicated that the shifts in cell proportions were unlikely to be driven by *PANTR1* dysregulation. In summary, *PANTR1* expression showed both increases and decreases across specific cell populations in *FOXG1* mutant organoids compared to controls, depending on the cell type.

FOXG1 binds the lincRNA *Pantr1*

Our interactome data from mouse and human FOXG1 revealed interaction with RBPs and thus post-transcriptional functions of FOXG1. In addition, members of the forkhead (Fkh) domain family bind to RNA [48], and one recent report shows that L1 mRNA is not only a transcriptional target of FOXG1 but also associated to FOXG1 [49]. Given these indications for FOXG1 complexing with RNA, we hypothesised about direct FOXG1/*PANTR1* binding and assessed potential colocalisation *in vivo*. We combined *PANTR1* single molecule (sm)FISH and FOXG1 immunostaining in hCO and mouse cortical sections and observed that the signals were close to each other within the nucleus in human and mouse cells (Fig. 4A and B, Supplementary Fig. S3A and B). We next used *catRAPID* [50] as a bioinformatics tool, which predicted interaction between FOXG1 and *Pantr1* in both mouse and human (Supplementary Fig. S3C). Applying RIP for FOXG1 followed by qPCR for *Pantr1* using mouse wild-type P0 brains identified *Pantr1* as a transcript among the precipitated RNAs (Fig. 4C). Equally, FOXG1 RIP from HD hCO precipitated *PANTR1*, levels of which decreased significantly upon *FOXG1* mutations (Fig. 4D). Additionally, we performed RIPseq for mouse FOXG1 and detected several RNAs that enriched in the FOXG1 RIP compared to the IgG control (Fig. 4E). Upon RIPseq, however, *Pantr1* was not among the top enriched RNAs, but it was present with only few reads compared to the most enriched RNA, *Map1b* (Supplementary Fig. S3D and E). For the reverse viewpoint, we used MS of hippocampal proteins precipitated through biotinylated *Pantr1*, which enriched a diverse set of proteins. However, we did not detect FOXG1 among them (Fig. 4F). Analysis of mouse FOXG1 interacting proteins [24] revealed overlapping FOXG1 interactors and *Pantr1* binding proteins

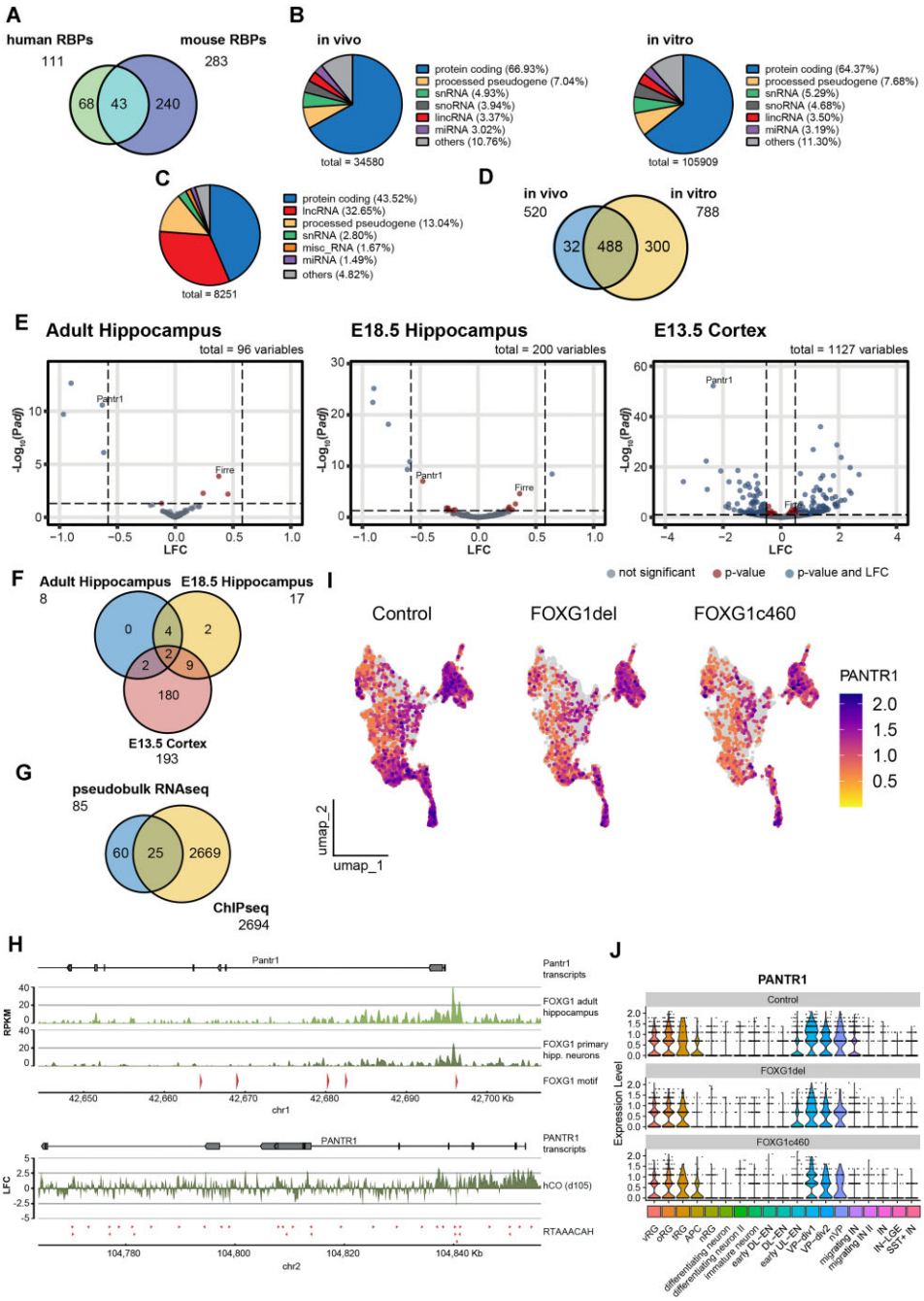

Figure 3. *Pantr1* is a direct FOXG1 target in mouse and human. (**A**) Venn diagram showing the overlap of RBP interactors identified in human (left) and mouse (right) FOXG1 interactome datasets, highlighting the shared RBPs between species. (**B**) Pie chart of the distribution of FOXG1 peaks regarding different subtypes of transcripts, derived from *in vivo* (adult, hippocampus) or *in vitro* (E18.5, cultivated hippocampal neurons) mouse ChIPseq data (GSE189119 [22]). (**C**) Pie chart of the distribution of FOXG1 peaks regarding different subtypes of transcripts, derived from hCO ChIPseq data (Fig. 2A and B). (**D**) Venn diagram of FOXG1 bound regions annotated as l(i)ncRNAs *in vivo* and *in vitro*, indicating an overlap of 488 between both conditions. (**E**) Volcano plots of differentially expressed l(i)ncRNAs upon *Foxg1* deletion in adult hippocampus ($Foxg1^{cre/+}$ versus wild-type mice, $n = 2$; GSE189119), E18.5 hippocampus ($Foxg1^{cre/+}$ versus wild-type mice, $n = 3$, GSE189119), and E13.5 cortex ($Foxg1^{cre/cre}$ versus wild-type mice, $n = 5$; GSE95833). The log2(fold change) (LFC) compared to the control on the *x*-axis, mean expression value of -log10 (*P*-value) on the *y*-axis. Dashed lines: threshold at adjusted *P*-value (padj) of 0.05 and an LFC of ± 0.58. DEGs fulfilling both conditions, or with a padj higher than 0.05 but an LFC between –0.58 and 0.58 or being non significant are highlighted. (**F**) Venn diagram of differentially expressed l(i)ncRNAs upon *Foxg1* deletion in adult hippocampus ($Foxg1^{cre/+}$ versus wild-type mice), E18.5 hippocampus ($Foxg1^{cre/+}$ versus wild-type mice), and E13.5 cortex ($Foxg1^{cre/cre}$ versus wild-type mice). (**G**) Venn diagram of differentially expressed l(i)ncRNAs in FOXG1del compared to HD hCO (pseudobulk RNAseq) and FOXG1 bound regions annotated as l(i)ncRNA as revealed by ChIPseq data from d105 hCO. (**H**) Top: ChIPseq of FOXG1 in wildtype *in vivo* adult hippocampus and *in vitro* E18.5 mouse primary hippocampal neurons (DIV11) [22] shows FOXG1 bound regions at the *Pantr1* gene. Upper track: overlay of all *Pantr1* transcript variants in this region, with position on chromosome 1 (chr1) in Kb on *x*-axis (mm10 genome). Given are reads per kilobase of transcript per million mapped reads (RPKM). Lower track: all potential FOXG1 binding sites with mouse FOXG1 motifs. Bottom: d105 hCO ChIPseq of FOXG1 shows FOXG1 bound regions at the *Pantr1* gene. LFC compared to the input is shown, with the position on chromosome 2 (chr2) in Kb (hg38 genome) on *x*-axis. Lower tracks shows all potential FOXG1 binding sites containing the motif RTAAACAH. (**I**) UMAPs of HD, FOXG1del, and FOXG1c460 organoids coloured by expression level of *PANTR1* (low: grey; high: purple to yellow). (**J**) Violin plots of cell-type specific expression distribution of *PANTR1* in HD, FOXG1del and FOXG1c460.

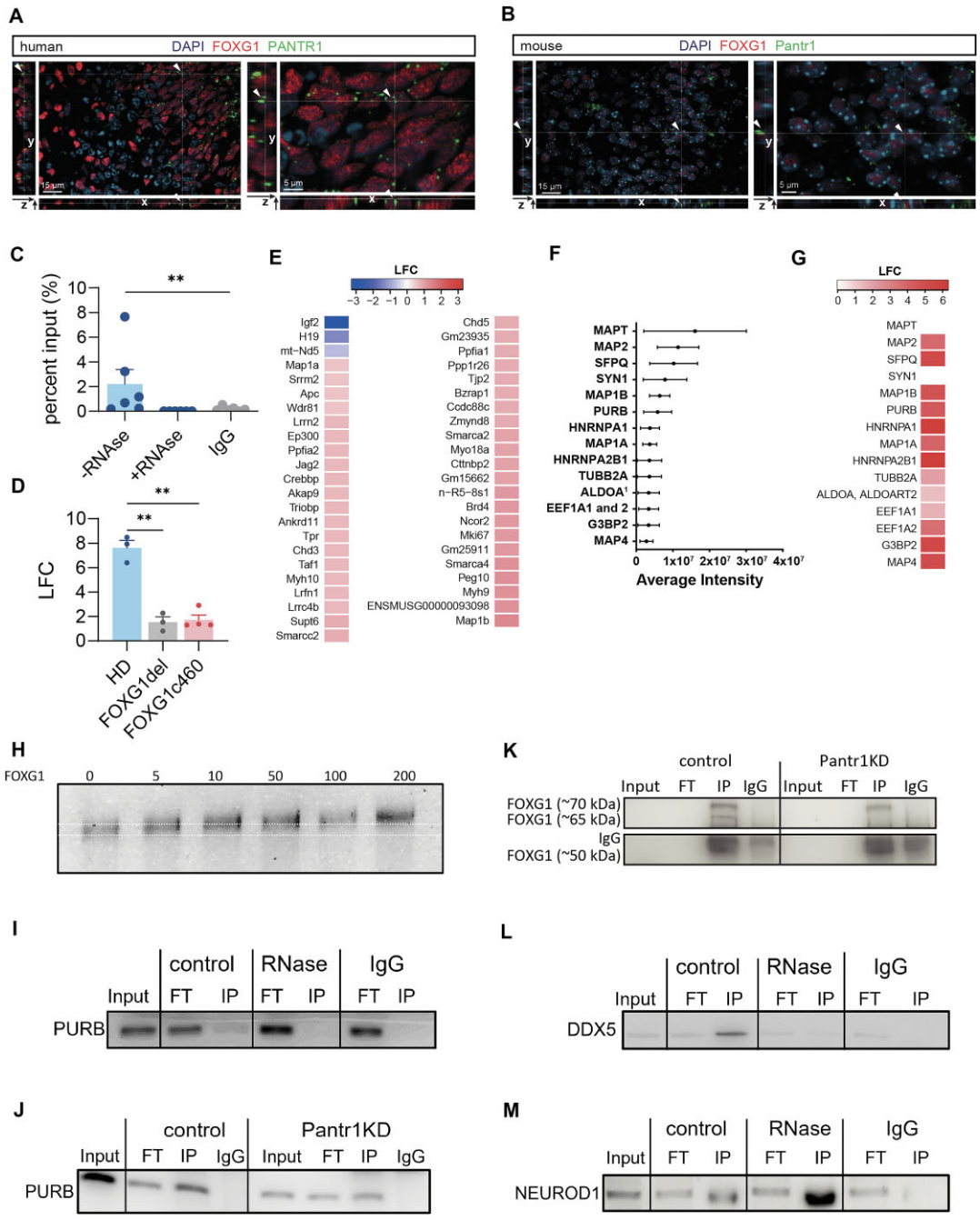

Figure 4. FOXG1 associates with *Pantr1*. (**A**) HD hCO stained with *PANTR1* smFISH probe and FOXG1 antibody, as orthogonal projections of confocal z-stacks. The orientation of the *x*-, *y*-, and *z*-axis is indicated, arrowheads point on colocalisation of *PANTR1* and FOXG1. (**B**) Mouse E18.5 brain stained with *Pantr1* smFISH probe and FOXG1 antibody, as orthogonal projections of confocal z-stacks. Orientation and arrowheads as in (**A**). Right: magnification of the left image. (**C**) FOXG1 RIP-qPCR in whole brain lysates from P0 wild-type mice. Percentage of input *Pantr1* RNA co-precipitated with FOXG1 or IgG, ± RNase. $n = 6$; ratio paired Student's t-test. *: $P < 0.05$. (**D**) FOXG1 RIP-qPCR in hCO from HD, FOXG1del, and FOXG1c460. LFC of input-normalised *PANTR1* enrichment in FOXG1 versus IgG immunoprecipitates. $n = 3$–4; Brown-Forsythe and Welch ANOVA. *: $P < 0.05$, **: $P < 0.01$, ***: $P < 0.001$. (**E**) Enriched genes after RIPseq using anti-FOXG1- compared to IgG-coated beads. Shown are the genes with adjusted P-value (padj) < 0.05 and a LFC < -0.584 or > 0.584. $n = 3$. (**F**) Proteins with the highest average intensity after MS analysis of *in vitro* transcribed *Pantr1* RNA pull down using 6-week adult mouse hippocampus protein lysates. Proteins with at least two identified peptides, coverage over 10% and *P*-value < 0.05 are given with average intensity and SEM. $n = 3$. (**G**) FOXG1 interactome enrichment of proteins binding *Pantr1* as in (**F**). FOXG1 interactome as published in [24]. (**H**) EMSA showing complex formation between *Pantr1* RNA and increasing concentrations of FOXG1 protein. Numbers indicate FOXG1:*Pantr1* molar ratios. Increasing FOXG1 concentrations result in progressive shift to higher molecular weight complexes, indicating dose-dependent binding of FOXG1 to *Pantr1*. (**I**) Co-IP of FOXG1 followed by PURB IB from P0 mouse hippocampus in control or RNase-treated conditions. PURB band at 40 kDa appears in input, flow through (FT), and bound to FOXG1 antibody conjugated beads (IP), but not in IgG control. (**J**) Co-IP of FOXG1 followed by PURB IB from primary hippocampal neurons (DIV7) expressing shCtrl (control) or shPantr1_1 (*Pantr1*KD). Loading as in (**I**). (**K**) Co-IP of FOXG1 followed by FOXG1 IB from primary hippocampal neurons (DIV7) expressing shCtrl (control) or shPantr1_1 (*Pantr1*KD). FOXG1 bands appear at 50, 65, and 70 kDa, of which 50 kDa is the size of regular FOXG1, 65 and 70 kDa represent FOXG1 isoforms or complexes with a cofactor. $n = 3$. (**L**) Co-IP of FOXG1 followed by DDX5 IB from P0 mouse cortex as in (**I**), with DDX5 band at 70 kDa. (**M**) Co-IP of FOXG1 followed by NEUROD1 IB from mouse hippocampus in control or RNase-treated conditions. NEUROD1 band at 49 kDa, labelling as (**I**).

(Fig. 4G). These findings suggested an association between FOXG1 and *Pantr1*, although it may occur directly, or be bridged by another protein. As FOXG1's functions in association with RNAs are only beginning to be recognised, we investigated both its potential direct interaction with *Pantr1*, and RNA-dependent associations involving proteins bound by both FOXG1 and *Pantr1*.

To this end, we isolated recombinant mouse FOXG1 protein from Sf9 cells (Supplementary Fig. S3F), which, upon elution, enriched as cytoplasmic 65 kDa isoform (Supplementary Fig. S3G). In EMSA, the recombinant FOXG1 shifted *in vitro* transcribed *Pantr1* (Fig. 4H). This showed direct interaction between FOXG1 and *Pantr1*.

To investigate the possibility of other partners being present in or bridging FOXG1/*Pantr1* interactions, we inspected the set of proteins associating with both, to shortlist potential candidates (Fig. 4G). This identified PURB, a protein binding lncRNAs in different cellular systems [51, 52]. Co-IP from mouse P0 brain extracts using FOXG1 antibody in presence or absence of RNase showed RNA-dependent interaction between FOXG1 and PURB (Fig. 4I). However, this interaction was not strictly dependent on *Pantr1*, because upon *Pantr1*KD in primary mouse hippocampal neurons, FOXG1 antibodies precipitated still PURB (Fig. 4J). Upon probing the immunoprecipitate for FOXG1 protein upon *Pantr1*KD, we detected FOXG1 in several bands, with molecular weights around 50, 65, and 70 kDa, of which the 65 kDa signal was undetectable upon *Pantr1*KD (Fig. 4K). This finding suggested a *Pantr1*-mediated occurrence of a specific $FOXG1^{65}$ isoform that coexisted with the monomeric $FOXG1^{50}$. The $FOXG1^{65}$ isoform could contain RNA, represent a specific, RNA-dependent conformation, or might be a heterodimer with a small 10–15 kDa protein. We also tested RNA-dependent FOXG1 interactions with two recently identified FOXG1 interacting proteins, namely DDX5 [24] and NEUROD1 [22]. While FOXG1/DDX5 interaction reduced upon presence of RNase (Fig. 4L), NEUROD1 increased in FOXG1 binding (Fig. 4M). Together, our findings establish direct binding of FOXG1 and RNA, i.e. *PANTR1,* as well as further RNA-dependent FOXG1 protein complexes.

FOXG1 and *Pantr1* synergise on transcriptional regulation of genes involved in neuronal differentiation

Pantr1 associated proteins (Fig. 4F) localised to both nucleus and cytoplasm. We assessed *Pantr1* localisation in primary hippocampal neurons and neural progenitor cells (NPCs) using smFISH combined with immunostainings, showing its cytoplasmic, dendritic, and nuclear localisation (Supplementary Fig. S4A–E). Combining our results so far, we hypothesised that FOXG1 and *Pantr1* might converge on transcriptional regulation. To explore altered transcriptomes, we transduced mouse DIV (days *in vitro*) 7 primary hippocampal neurons with shRNAs to KD either *Foxg1, Pantr1,* or luciferase control. We confirmed the KD by qPCR (Fig. 5A). KD of *Foxg1* let to 2971 DEGs, of which 1203 increased and 1768 decreased compared to the control, as determined by RNAseq and using a threshold of $\pm$ 0.58 log2(fold change) (LFC) and padj $\leq$ 0.05. For shPantr1, we identified in total 1800 DEGs (1254 decreased, 546 increased) compared to control (Fig. 5B). Whereas *Pantr1* was among the decreased DEGs (LFC= -0.435, padj = 0.020) upon *Foxg1*KD, *Foxg1* was not among the DEGs upon *Pantr1*KD (LFC = 0.036, padj = 0.755), confirming FOXG1 as an upstream regulator of *Pantr1*. This finding was also evident from RT-qPCRs upon KD of the respective gene (Fig. 5C). In total, we detected 2149 genes unique to *Foxg1*KD, 978 to *Pantr1*KD, and 822 genes were affected in common in both KD conditions (Fig. 5D and E). With the 822 common DEGs, 232 increased and 532 decreased in both KD conditions, whereas 47 increased upon *Foxg1*KD, but decreased upon *Pantr1* reduction, and 11 decreased in *Foxg1*KD, but increased upon *Pantr1*KD. GO-term enrichment analysis showed that decreasing DEGs upon *Foxg1*KD or *Pantr1*KD were functionally involved in neuronal differentiation (Fig. 5F). As suspected, the transcriptional changes upon *Foxg1*KD or *Pantr1*KD indicated a common regulative network impacting neuronal differentiation in the mouse hippocampus.

Pantr1 localises FOXG1 at specific binding sites at the chromatin level

Since (i) RIP-qPCR, RIPseq, and EMSA results showed binding of FOXG1 and *Pantr1*, and (ii) FOXG1 and *Pantr1* had common transcriptional targets, we hypothesised that *Pantr1* could potentially affect the localisation of FOXG1 at the chromatin level. To test this hypothesis, we performed ChIPseq of FOXG1 upon *Pantr1*KD in primary hippocampal neurons and identified indeed significantly differentially bound regions (DBRs) of FOXG1 compared to controls (Fig. 6A for significant peaks; all called FOXG1 peaks displayed in Supplementary Fig. S5A). Among the significant DBRs 233 increased and 21 decreased FOXG1 binding upon *Pantr1* reduction. To the largest part, DBRs had promoter or distal intergenic features (Fig. 6B). GO-term enrichment retrieved functional terms associated with neuronal differentiation (Fig. 6C; all called FOXG1 peaks displayed in Supplementary Fig. S5B), in accordance with the observed transcriptional regulations upon reduced expression of FOXG1. We identified 13 shared DEGs that also harboured significant DBRs (Supplementary Fig. S6), which rendered these as *Pantr1*-dependent FOXG1 target genes (Fig. 6D; common DEGs after *Foxg1*KD and DBRs upon *Pantr1*KD displayed in Supplementary Fig. S5C). Expression of these *Pantr1*-dependent FOXG1 targets increased or decreased, and this bimodal impact of FOXG1 on transcription was in accordance with our previous observations [22]. We also observed enrichment of FOXG1 in human d105 hCO in most of the 13 mouse ChIPseq target genes. In part, the FOXG1 enrichment was found at sites for which we identified homology between human and mice, and which were differentially bound by FOXG1 upon *Pantr1*KD in mouse cells (Supplementary Fig. S7A). It is thus tempting to speculate that *PANTR1* is involved in site-specific FOXG1 localisation in humans in similar manner as observed in the mouse. Supporting this hypothesis is the finding that *SLC8A1*, an important mediator of intracellular sodium/calcium homeostasis [53], decreased in both human and mouse models with reduced levels of FOXG1 (Fig. 6D, Supplementary Fig. S7B).

We performed a differential transcription factor DNA-binding motif enrichment analysis for the significant FOXG1 DBRs upon *Pantr1*KD in mouse hippocampal cells. Increased binding of FOXG1 occurred at sites that were enriched in GC- and GAA-rich motifs, characteristic for Zinc-finger- or heat shock transcription factors, in addition to generic Fkh-binding motifs encompassing the entire Fkh family (Fig. 6E). On the other hand, regions with NEUROD- (bHLH) binding

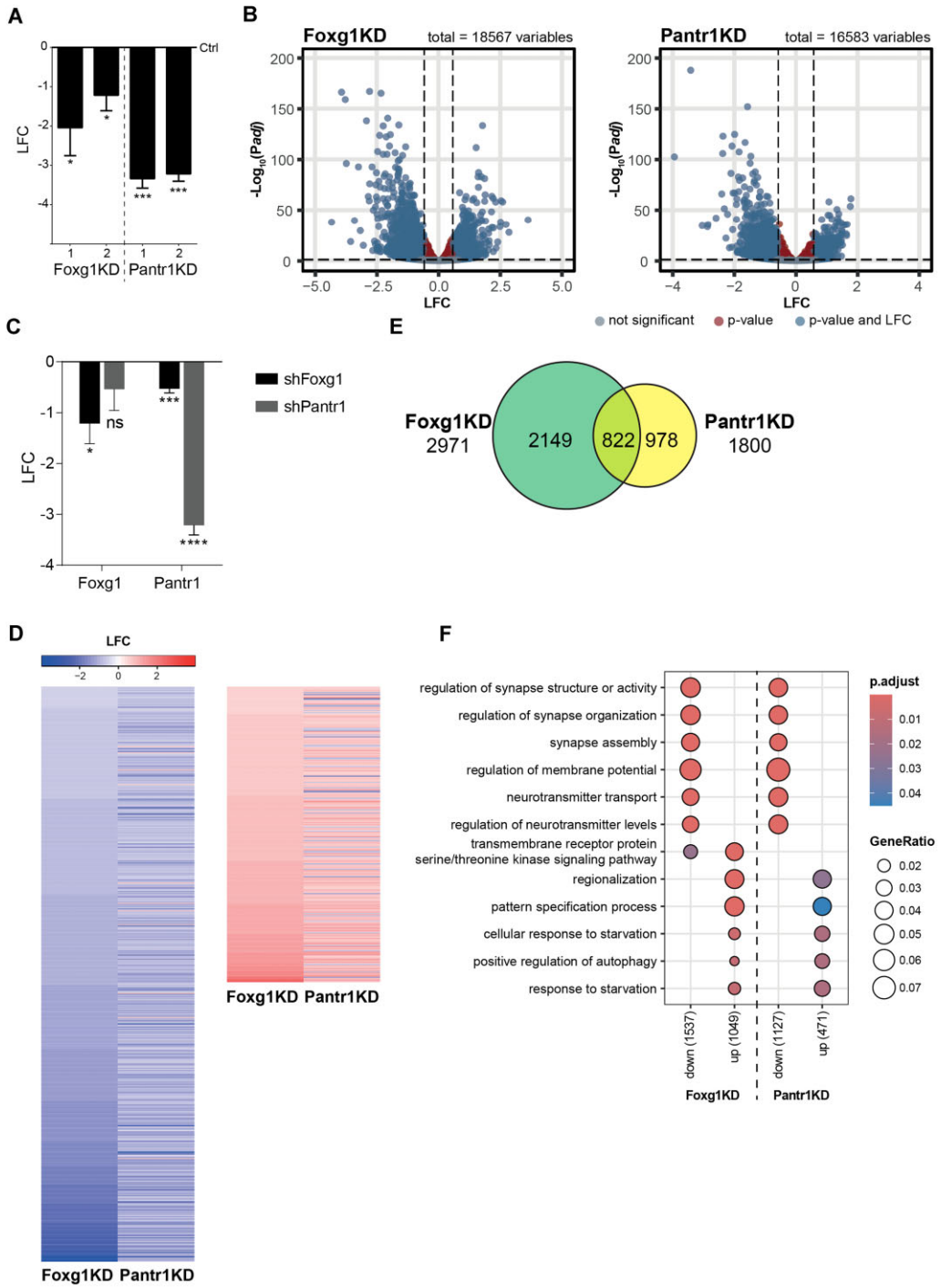

Figure 5. FOXG1 and *Pantr1* share transcriptional target genes impacting neuronal differentiation. (**A**) Primary hippocampal neurons DIV7 transduced with either shCtrl or shRNAs targeting *Foxg1* or *Pantr1*. All transcript levels decreased significantly upon KD with the respective shRNAs (shFoxg1_1, shFoxg1_2; and shPantr1_1, shPantr1_2) compared to shCtrl, as assessed by qPCR with *Gapdh* as housekeeping gene. Given is the log2(fold change) (LFC) of the expression in shRNA treated cells (*Pantr1*KD and *Foxg1*KD) compared to shCtrl treated cells (Ctrl). $n = 3$ (shFoxg1_1 and shPantr1_1), $n = 4$ (shFoxg1_2 and shPantr1_2). Unpaired Student's t-test to Ctrl: * $P < 0.05$, ** $P < 0.01$, *** $P < 0.001$. (**B**) Volcano plots of DEG in DIV7 primary hippocampal neurons transduced with shFoxg1_1 (*Foxg1*KD) compared to shCtrl (Ctrl), and shPantr1_1 (*Pantr1*KD) compared to shCtrl (Ctrl). The log2(fold change) (LFC) compared to the control is shown on the *x*-axis while the *y*-axis is showing the mean expression value of -log10 (*P*-value). Genes with increased or decreased expression and an adjusted *P*-value (padj) < 0.05 and additionally LFC < -0.584 or > 0.584 based on the Deseq2 analysis results are indicated. $n = 5$. Dashed lines are indicating the thresholds for padj (0.05) and LFC (−0.584 and 0.584). (**C**) RT-qPCR analysis showing log2(fold change) (LFC) of *Foxg1* and *Pantr1* expression following KD with shFoxg1 or shPantr1 in mouse hippocampal neurons. *Foxg1* KD significantly reduced both *Foxg1* and *Pantr1* expression. *Pantr1*KD significantly reduced *Pantr1* expression without significantly affecting *Foxg1* levels. $n = 4$. Data are presented as mean ± SEM; *: $P < 0.05$, **: $P < 0.01$, ***: $P < 0.001$, ****: P< 0.0001; ns: not significant. (**D**) Heatmap of DEGs upon *Foxg1*KD and *Pantr1*KD in primary hippocampal neurons. Given is the log2(fold change) (LFC) for common DEGs with an adjusted P-value (padj) < 0.05 and a LFC <−0.584 or >0.584. $n = 5$. (**E**) Venn diagram of DEGs upon KD of *Foxg1* or *Pantr1* with an adjusted *P*-value (padj) < 0.05 and a LFC <−0.584 or >0.584, indicating a set of 822 commonly regulated target genes. $n = 5$. (**F**) GO-term enrichment analysis of DEGs upon KD of *Foxg1* or *Pantr1* split according to DEGs with either increased or decreased expression compared to shCtrl. Given are the top enriched GO terms with a FDR > 0.5.

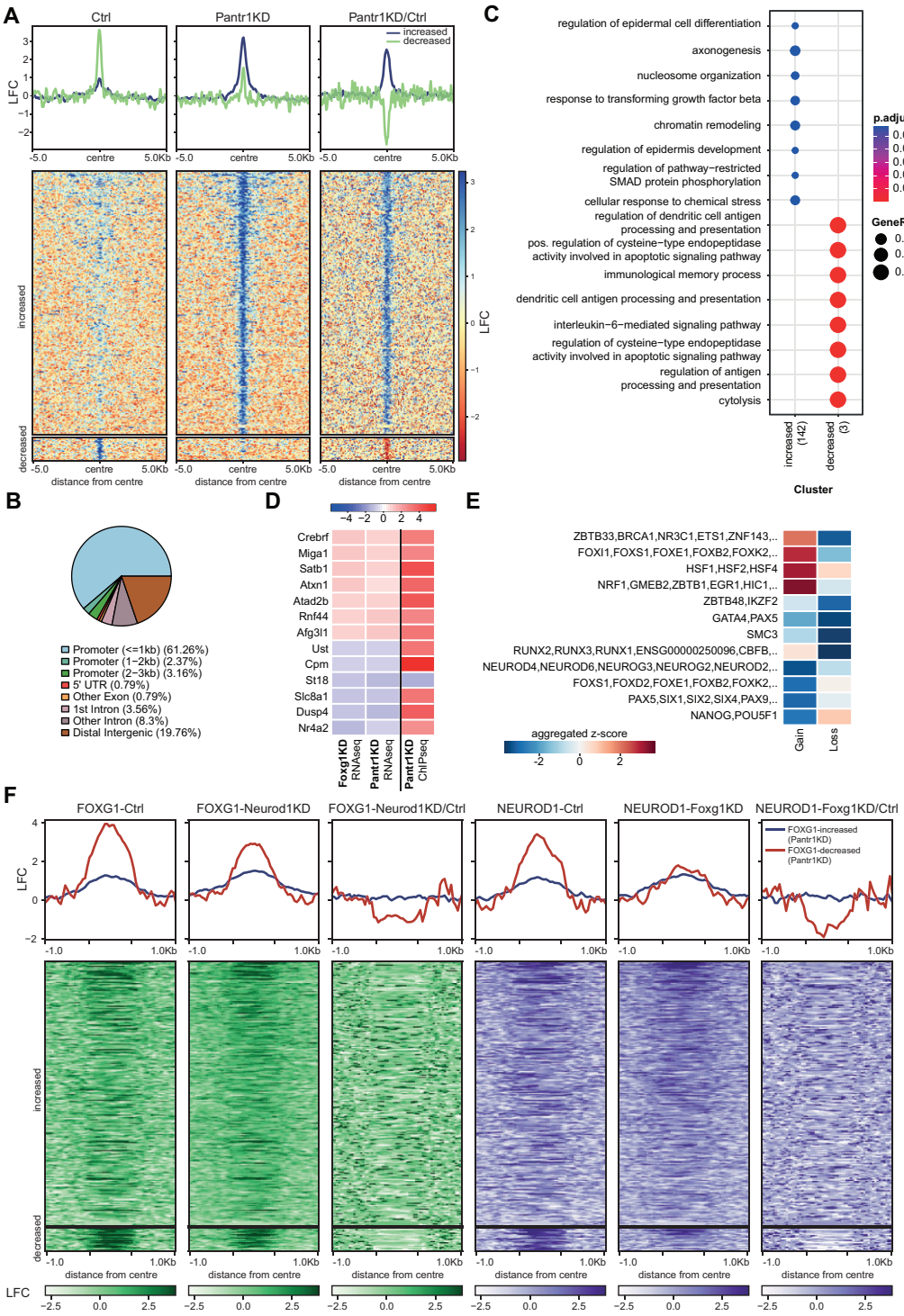

Figure 6. *Pantr1* regulates FOXG1 presence at the chromatin. (**A**) Heatmap of differently bound regions (DBRs) of FOXG1 upon *Pantr1*KD, 5 Kb up-/downstream of FOXG1 peak summits in control and *Pantr1*KD conditions. DBRs were calculated using Diffbind. Data are normalised by sequencing depth and input control as log2(ChIP/Input) for control and *Pantr1*KD data. The difference between *Pantr1*KD and control conditions was calculated from RPKM normalised bigwig files as log2(*Foxg1*KD/Control). The metaprofiles (top) show the mean log2(fold change) (LFC) of increased and decreased regions. $n = 2$. (**B**) Genome-wide distribution of DBRs of FOXG1 upon *Pantr1*KD in DIV7 primary hippocampal neurons in percentage for near and far promotor regions, 5′UTR, intronic and exonic as well as distal intergenic regions. (**C**) GO-term enrichment of differentially bound regions of FOXG1 upon *Pantr1*KD in DIV7 primary hippocampal neurons with a qvalue cutoff of 0.05 and pvalue cutoff of 0.05. (**D**) Heatmap of common DEGs in the RNAseq data sets after *Pantr1*KD and *Foxg1*KD (adjusted *P*-value (padj) < 0.05 and a LFC < -0.584 or > 0.584) and annotated genes (ChIPSeeker) corresponding to the significant DBR in the FOXG1-ChIPseq data set after *Pantr1*KD. Shown are the LFC (RNAseq) or fold change (ChIPseq) compared to the control condition. (**E**) Motif analysis of the increased (gain) and decreased (loss) DBRs. Shown is the aggregated *z*-score. (**F**) Heatmap of FOXG1 (left three panels) and NEUROD1 (right three panels) enrichments at the increased and decreased DBRs under control, *Neurod1*KD, and *Foxg1*KD conditions. Data were obtained from [22] and were normalised by sequencing depth and input control as log2(ChIP/Input). The difference between *Foxg1*KD-Control and *Neurod1*KD-Control conditions were calculated from RPKM normalised bigwig files as log2(*transcription factor* KD/Control). The metaprofiles (top) show the average log2(fold change) (LFC) of increased and decreased regions. $n = 2$.

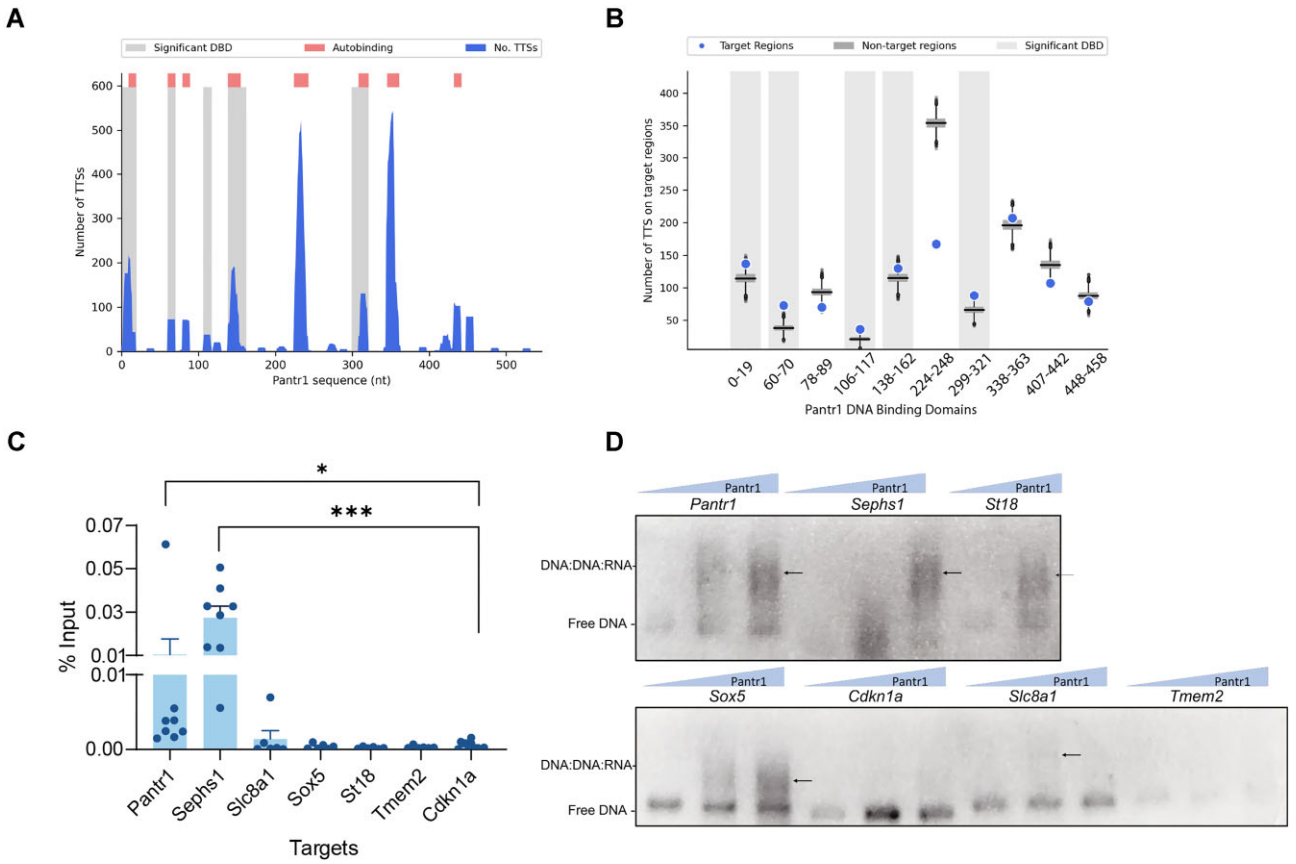

Figure 7. *Pantr1* binds directly DNA at FOXG1 binding regions. (**A**) The potential of *Pantr1* to form RNA–DNA triplexes was assessed using the TDF module from the RGT-Regulatory Genomics Toolbox. Highlighted blocks indicate *Pantr1* domains with significant prediction to form triplex structures with genomic DNA (significant DBD). Squares on top denote predicted binding of the *Pantr1* transcript to its own genomic locus (Autobinding). (**B**) The binding potential of *Pantr1* was assessed at differential FOXG1 peaks identified upon *Pantr1*KD in ChIP-seq (from Fig. 6A). Dots indicate genomic target regions within the input set that are predicted to be bound by the specified DBDs of *Pantr1* via triplex formation. (**C**) ChIRP-qPCR showing *Pantr1* enrichment at selected genomic loci from (**B**) in P0 mouse cortical tissue. Significant enrichment was detected for *Pantr1* and *Sephs1*, indicating direct chromatin association. Data are presented as % input (mean ± SEM). $n = 4$; odd and even probe sets were pooled, resulting in eight data points per target. Statistical analysis was performed using the Kruskal–Wallis test with Dunn's multiple comparisons. *: $P < 0.05$, **: $P < 0.01$, ***: $P < 0.001$. (**D**) DNA:RNA hybridisation mobility shift assay using *in vitro* transcribed *Pantr1* RNA and target DNA amplicons from (**C**). A shift to higher molecular weights upon RNA addition confirms direct hybridisation between *Pantr1* RNA and target DNA fragments for *Pantr1*, *Sephs1*, *St18*, *Sox5*, and *Slc8a1*.

sites or palindromic Fkh motifs, bound specifically by FOXO and FOXA family members, were fewer among the motifs under bound sites (Fig. 6E, Supplementary Fig. S5D for all called peaks). These findings suggested that upon *Pantr1*KD, FOXG1 was redistributed at the chromatin, seemingly favouring generic sites harbouring a variety of motifs.

Motifs conferring binding sites of transcription factors known to interact with FOXG1, including FOXO members and NEUROD1, were comparably less represented in the regions gaining FOXG1 binding upon *Pantr1*KD. We recently reported on the cooperative presence of FOXG1 and NEUROD1 at several FOXG1 bound regions [22], and observed decreased occurrence of FOXG1 binding at NEUROD motifs upon *Pantr1*KD. Therefore, we hypothesised that regions where FOXG1 binds in a *Pantr1*-dependent manner also exhibited a specific pattern of NEUROD1 binding. To test this hypothesis, we specifically analysed *Pantr1*-dependent FOXG1 bound regions in the NEUROD1 ChIPseq dataset. At DBRs with increased binding of FOXG1 upon *Pantr1*KD, we did not observe significant alterations in the binding pattern of FOXG1 or NEUROD1 upon KD of either *Foxg1* or *Neurod1*. However, focusing on regions where FOXG1 binding decreased upon *Pantr1*KD, we observed a corresponding reduction in NEUROD1 binding upon *Foxg1*KD and a decrease in FOXG1 binding upon *Neurod1*KD (Fig. 6F). Together, these findings suggested that in mice, *Pantr1* facilitates cooperative presence of FOXG1/NEUROD1 at specific sites, and *Pantr1* reduction leads to redistribution of FOXG1 to comparably more generic binding sites.

We hypothesised a direct association of *Pantr1* with DNA to regulate FOXG1 binding site selection. We used the *TDF* tool from the *RGT-Regulatory Genomics Toolbox* [44] that predicted five significant DNA-binding regions within the *Pantr1* RNA, involved in forming triplex target sites (TTS) (Fig. 7A). Next, we used the same tool to assess the probability of *Pantr1* binding to FOXG1 binding sites that altered upon *Pantr1*KD. This analysis revealed that the five *Pantr1* DNA-binding sites showed binding probability to various corresponding FOXG1-binding regions (Figs 6A, 7B). Only four of the predicted chromatin-binding sites for *Pantr1* overlapped with regions showing decreased FOXG1 binding upon *Pantr1*KD, while the majority of normalised TTS signals were located in regions with significantly increased FOXG1 binding. This suggested that *Pantr1*-mediated DNA:RNA hybrids

at FOXG1 peaks limited FOXG1 binding to the chromatin. We selected a subset of regions potentially bound by *Pantr1* based on normalised TTS counts, sum-of-ranks parameters, and primer design feasibility. ChIRP (chromatin isolation by RNA purification)-qPCR performed on these regions revealed significant enrichment of *Pantr1* and *Sephs1*, confirming *Pantr1* binding at a subset of the predicted sites (Fig. 7C). Amplicons of these target regions were also used in an *in vitro* DNA:RNA hybridisation shift assay. This assay further confirmed that *Pantr1* directly bound to the *Pantr1, Sephs1, St18, Sox5*, and *Slc8a1* target sequences, as the addition of *Pantr1* RNA caused a shift of these DNA fragments to higher molecular weights (Fig. 7D), supporting a direct association between *Pantr1* and chromatin.

Pantr1 OE upon reduced expression of *Foxg1* rescues dendritic outgrowth defects

Since GO-term enrichment suggested that impaired neuronal differentiation might be a common feature of reduced expression of *Foxg1* or *Pantr1*, we transduced primary hippocampal neurons with the respective shRNAs, cultured them until DIV7 and quantified dendritic branching and outgrowth using Sholl-analysis. The number of dendrites decreased 10–100 μm proximal to the soma upon either *Foxg1*KD or *Pantr1*KD condition compared to control (Fig. 8A and B). Further, we tested whether *Pantr1*KD would impair spine density and spontaneous excitatory post-synaptic currents (sEPSC), as reported for *Foxg1* loss-of-function [16]. Indeed, we observed a reduced spine density in transduced primary hippocampal cells that expressed shPantr1 alongside a GFP reporter construct compared to control condition (Fig. 8C and D). This decrease in spine density was associated with reduced spontaneous firing rates (Fig. 8E), decreased sEPSC amplitudes (Fig. 8F) and a lower frequency of sEPSCs (Fig. 8G) following *Pantr1*KD compared to controls. These findings are consistent with a downregulation of *Gria2* and *Gria4* expression upon *Pantr1*KD as indicated by the transcriptome data (Fig. 8H).

Our data suggested that reduced expression of FOXG1 decreased *Pantr1* expression, and that the regulative network centred on both factors impacted dendritic outgrowth in hippocampal neurons. The upstream action of FOXG1 implied that OE of *Pantr1* would be a means to rescue - at least in part - loss of FOXG1 function. To address this potential functional interplay between FOXG1 and *Pantr1*, we expressed either shFoxg1 alone, overexpressed *Pantr1* or expressed shFoxg1 alongside *Pantr1* OE in primary hippocampal neurons. Sholl-analysis of hippocampal neurons showed a mild, but still observable decrease in dendritic arborisation upon *Foxg1*KD, but significant increase upon *Pantr1*OE in the condition of *Foxg1*KD, compared to the control (Fig. 8I). The rescue effect was strongest in a range near the soma, between 10 and 60 μm (Fig. 8I and J). These data suggested that in the context of dendritic development *Pantr1* acts downstream of FOXG1 to regulate this aspect of neuronal differentiation in mouse hippocampal neurons.

Discussion

Our investigation into the role of l(i)ncRNAs in the context of FOXG1-syndrome led to identifying *Pantr1* as one of the crucial lincRNAs that shows altered expression levels across various model systems exhibiting *Foxg1*-haploinsufficiency or full deletion. Here, we report a functional synergy between FOXG1 and *Pantr1*, manifested through two distinct molecular mechanisms in our study. For one, our transcriptomic and functional characterisations place FOXG1 as an upstream regulator of *Pantr1* expression in the cerebral cortex and hippocampus of the mouse as well as in hCO. In hCO, FOXG1 mutation impaired proper *PANTR1* expression especially in distinct IN stages. It might be tempting to speculate that dysregulated *PANTR1* levels correlate with the disbalance of excitatory and inhibitory activity in iPSC-derived model systems of human FOXG1-syndrome patients [2, 17]. Notably, in the context of the human FOXG1-syndrome, OE of *Pantr1* in mouse hippocampal neurons with reduced FOXG1 levels rescued dendritic complexity. This finding renders the lincRNA *Pantr1* as an important mediator of FOXG1 function in promoting the correct formation of the dendritic tree in the mouse. It might also be a potential target for testing therapeutic options in humans for FOXG1-syndrome, but also beyond, since both *PANTR1* and FOXG1 are implicated in glioblastoma pathology [54, 55]. However, much more research on *PANTR1* functions, especially in the human system in the different cell subtypes, is needed in further upcoming studies.

The second molecular mechanism through which FOXG1 and *Pantr1* converge arises from our observation that FOXG1 binds *Pantr1*. Together with recent evidence showing that FOXG1 associates with L1 mRNA [49], this suggests an emerging model in which FOXG1 engages in both DNA and RNA interactions, despite lacking canonical RNA-binding motifs. Recent reports link RNA binding to other features than classical RNA-binding domains, including intrinsically disordered regions (IDR), and they suggest interaction of DNA and/or DNA-binding proteins with RNA-binding proteins (RBP) [56–58]. Along these lines, the Fkh protein domain has been recognised mainly as DNA-binding so far, but recently it has been also reported to confer association with RNA by binding to G2-rich sequences, being composed of a consensus sequence containing 8 GG nucleotides interspersed by one or two different nucleotides [48]. We did not identify a G2-rich consensus within the sequences of human *PANTR1* (ENST00000443988.7, PANTR1-202) or mouse *Pantr1* (ENSMUSG00000060424, all exons). The *Pantr1*-binding capability of FOXG1 might therefore be encoded in its extensive IDR, as predicted by using disoFLAG [59]. Despite our EMSA data indicating direct association between FOXG1 and *Pantr1*, different modes of binding cannot be ruled out completely, as these partners share common protein binding partners. Among these we studied PURB, which did not lose its interaction with FOXG1 upon *Pantr1*KD, but lost it in presence of RNase. Similar to PURB, DDX5 and NEUROD1 interactions with FOXG1 are RNA dependent, indicating that FOXG1 uses RBPs to extend its functional repertoire to a plethora of post-transcriptional processes.

Our study showed further that presence of *Pantr1* coincided with a specific FOXG1 protein isoform, with a slightly higher molecular mass, i.e. $FOXG1^{65}$, compared to slightly lower, predicted mass of FOXG1 in $FOXG1^{50}$. Association with a small, 10–15 kDa protein could explain this shift in mass. However, neither the interactome nor RIP followed by MS studies suggested a common top enriched protein with 10–15 kDa that could account for the difference between $FOXG1^{50}$ and $FOXG1^{65}$. It thus remains to be explored whether $FOXG1^{65}$ contains RNA, represents a stable con-

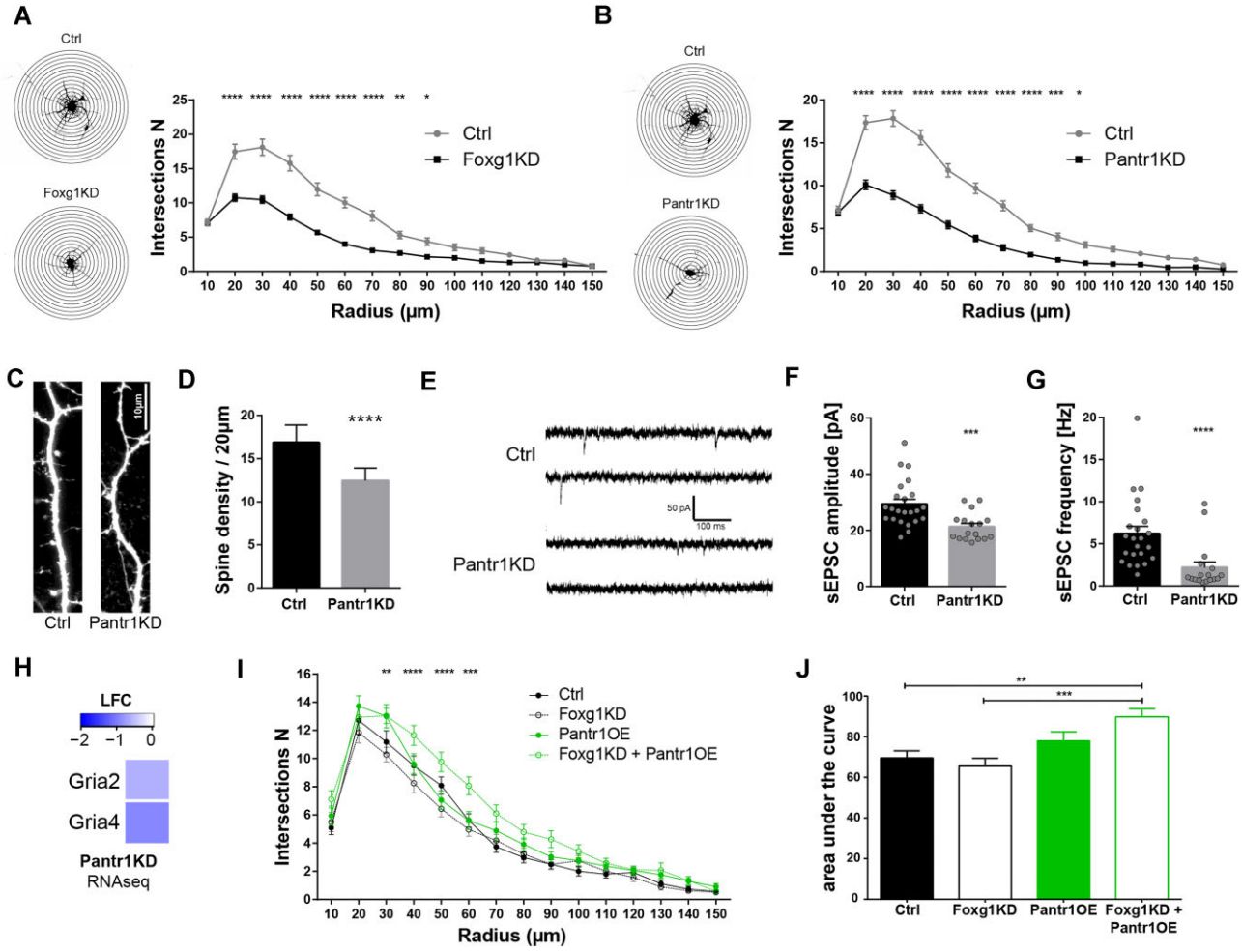

Figure 8. *Pantr1* partially rescues neuronal differentiation defects upon FOXG1 reduction. (**A** and **B**) Camera lucida reconstruction of representative DIV7 primary neurons after transduction with shCtrl (Ctrl), shFoxg1 (Foxg1KD) or shPantr1 (*Pantr1*KD) and superimposed concentric circles used for Sholl-analysis. The radius interval between the circles was 10 µm per step. Quantification of Sholl-analysis of control (shCtrl) and *Foxg1*KD (**A**, combined for shFoxg1_1 and 2) or *Pantr1*KD (**B**, combined for shPantr1_1 and 2), showing significantly decreased dendritic complexity upon *Foxg1*KD (shCtrl: $n = 45$, shFoxg1_1 and 2: $n = 76$) or *Pantr1*KD (shCtrl: $n = 65$, shPantr1_1 and shPantr1_2: $n = 53$). Two-way ANOVA, Sidak multiple comparison test. *: $P < 0.05$, **: $P < 0.01$, ***: $P < 0.001$, ****: $P < 0.0001$. (**C**) Representative images of spines from dendritic branches upon shCtrl and shPantr1_1. Biocytin-filled neurons were stained with Alexa Fluor™ 633-conjugate. Scale bar: 10 µm. (**D**) Quantification of spines in 20 µm increments of stained dendrites as shown in C, showing that spine density reduced significantly in *Pantr1*KD condition (shCtrl: 13 cells from 4 cultures; shPantr1_1*:* 19 cells from 4 cultures, unpaired Student's t-test, ****: $P < 0.0001$). (**E**) Representative traces of spontaneous excitatory postsynaptic currents (sEPSCs) from shCtrl or shPantr1_1 transduced hippocampal neurons recorded on DIV14. (**F, G**) Group data of mean sEPSC amplitude (**F**) and frequency (**G**) from *Ctrl* and *Pantr1*KD neurons recorded on DIV14. shCtrl: $n = 23$, shPantr1_1: $n = 17$. Significance was determined by Mann–Whitney test, ***$P < 0.001$, ****$P < 0.0001$. (**H**) Heatmap of log2(fold change) (LFC) expression level changes of *Gria2* and *Gria4* upon *Pantr1*KD in DIV7 hippocampal neurons compared to controls as revealed by RNAseq analysis. (**I**) Sholl analysis of dendrite complexity upon *Foxg1*KD, *Pantr1* OE and combination of *Foxg1*KD and *Pantr1*OE compared to Ctrl, showing that *Pantr1*OE rescues reduced dendritic complexity upon FOXG1 reduction (Ctrl $n = 34$, *Foxg1*KD $n = 32$, Pantr1OE $n = 33$, *Foxg1*KD_*Pantr1*OE $n = 29$). The radius interval between the circles was 10 µm per step. Two-way ANOVA with Sidak multiple comparison test was performed over all conditions. Shown is the significance of *Foxg1*KD_*Pantr1*OE versus *Foxg1*KD, **$P < 0.01$, ***$P < 0.001$, ****$P < 0.0001$. (**J**) Bar chart representation of quantifications given in **I**. Given is the sum of intersections of all intervals as area under the curve for control cells and cells with *Foxg1*KD, *Pantr1* OE and the combination of *Foxg1*KD and *Pantr1*OE. One-way ANOVA with Tukey's multiple comparison test was performed over all conditions, **$P < 0.01$, ***$P < 0.001$.

formation, or has a small, but currently undetected protein interactor.

The enrichment of cytoplasmic binding partners of FOXG1 and/or *Pantr1* could result from a technical bias, for example caused by predominant extraction of cytoplasmic proteins for the *Pantr1* binding assay. On the other hand, predominant cytoplasmic interactors can reflect that FOXG1 would be sequestered in the cytoplasm through *Pantr1*. A sequestering function of *Pantr1* for FOXG1 could explain the increased binding of FOXG1 to chromatin upon *Pantr1*KD. However, the sponging being the sole purpose of FOXG1/*Pantr1* complexes is not well supported by two of our observations: (i) the nuclear colocalisation of FOXG1 and *Pantr1 in vivo*, and (ii) *Pantr1*'s sponging effect on FOXG1 protein in the cytoplasm would scarcely account for the selectivity observed in differentially bound chromatin regions of FOXG1 upon *Pantr1*KD.

The limited number of loci, with mainly increased FOXG1 binding upon *Pantr1*KD, rather suggests that *Pantr1* is involved in localising FOXG1 and confers site-specific transcription factor binding. In this context, our data suggest that

Pantr1 does not interfere with *de novo* binding of FOXG1 to the chromatin, as sites with increased binding had FOXG1 peaks also in the control condition. Rather our data indicate that *Pantr1* limits (i) FOXG1 presence at already bound regions (Supplementary Fig. S5) and (ii) spreading of FOXG1 to generic binding sites (Fig. 6E). In support of *Pantr1* limiting FOXG1 chromatin binding, *Pantr1* binds the FOXG1 target regions by its significantly predicted DBDs. The majority of DBRs upon *Pantr1*KD exhibited increased FOXG1 binding, indicating that *Pantr1* exerts a predominantly antagonistic effect on FOXG1 chromatin occupancy. These findings are consistent with a model in which *Pantr1* forms DNA:RNA hybrids (R-loops) at FOXG1 peaks with generic binding motifs to block FOXG1 binding. Removal of *Pantr1* relieves this steric hindrance, allowing FOXG1 access. On the other hand, *Pantr1* might facilitate cooperative localisation of FOXG1 and NEUROD1, as the regions where FOXG1 binding decreased upon *Pantr1*KD coincide with regions where loss of either FOXG1 or NEUROD1 affects the localisation of the other transcription factor (Fig. 6F). Importantly, co-IP experiments revealed that FOXG1–NEUROD1 interaction increases upon RNase treatment, suggesting that RNA, maybe including *Pantr1*, obstructs their physical interaction, at least, in lysates. The data on RNA-dependent interaction of FOXG1 with other TFs are to scarce as of yet to go beyond speculation that all components are required for their functional cooperation at the chromatin, but it seems emerging that *Pantr1* is required for FOXG1/NEUROD1 functional cooperation at chromatin.

In conclusion, based on our data, we propose that *Pantr1* has diverse roles in modulating FOXG1 presence at the chromatin. At FOXG1 binding sites containing generic binding motifs, *Pantr1* acts as a repressor by forming R-loops that block FOXG1 binding. In addition, *Pantr1* affects FOXG1 binding at sites with cooperative FOXG1/NEUROD1 binding, where KD of FOXG1 or NEUROD1 affects presence of the other partner. At these sites, *Pantr1* has a promoting effect on FOXG1 binding. Off-chromatin, RNA molecules limit FOXG1/NEUROD1 complex formation, indicating a context-dependent regulatory role of RNA in modulating this FOXG1 interaction and potential genomic targeting of FOXG1/NEUROD1 complexes.

Clearly, much more research is needed to unravel how FOXG1 localisation within cellular compartments, at the chromatin level, and in association with RNAs is regulated. Evidently, our study of *Pantr1* localisation and interaction with putative other protein partners suggest a plethora of additional functions for *Pantr1* as well as FOXG1 in the cytoplasm and nucleus that await further research.

Acknowledgements

The authors thank S. Heidrich for technical assistance. We also thank A. Izzo for scientific support and critical comments on the manuscript. We thank E. Gabriel and J. Gopalakrishnan, Heinrich-Heine-University Düsseldorf, Germany, for scientific support in the generation of organoids. The authors thank M. Börries, Institute of Medical Bioinformatics and Systems Medicine, University Medicine Freiburg, for infrastructural support of the study. The authors thank S. Tholen of the Proteomic Platform – Core Facility (ProtCF), which was supported by the Medical Faculty of the University of Freiburg to O. Schilling (2021/A3-Sch and 2023/A3-Sch). The authors acknowledge the support of the Freiburg Galaxy Team: P. Videm and B. Grüning, Bioinformatics, University of Freiburg, Germany, funded by the German Federal Ministry of Education and Research BMBF grant 031 A538A de.NBI-RBC and the Ministry of Science, Research and the Arts Baden-Württemberg (MWK) within the framework of LIBIS/de.NBI Freiburg. We also thank U. Bönisch, MPI Immunobiology and Epigenetics, Freiburg, Germany, from the sequencing core facility. Control hiPSCs were provided by the FiPS Core Facility, University Medicine Freiburg, Germany. The "Cell lines and DNA bank of Rett Syndrome, X-linked mental retardation and other genetic diseases", member of the Telethon Network of Genetic Biobanks (project no. GTB12001), funded by Telethon Italy and of the EuroBioBank network, provided us with hiPSC with FOXG1 deletion and c460dupG frameshift mutation.

Author contributions: T.V. conceived and designed the study. Material preparation, data collection, and analysis were performed by F.G., T.R., I.A., C.L.F., G.A., and T.V. R.G-F., A.F., A.V., and R.B. supervised and guided experiments and/or analyses. The first draft and the revision of the manuscript were written by T.V. together with F.G. and I.A., and all authors read and approved the final manuscript. F.G. (Data curation [equal], formal analysis [equal], investigation [equal], project administration [equal], validation [equal], writing – review & editing [equal]), T.R. (Formal analysis [equal], methodology [equal], visualization [equal], writing – review & editing [equal]), I.A. (Data curation [equal], formal analysis [equal], investigation [equal], methodology [equal], project administration [equal], validation [equal], visualization [equal], writing – review & editing [equal]), G.A. (Formal analysis [supporting], investigation [supporting], methodology [supporting], visualization [supporting], writing – review & editing [supporting]), C.L.F. (Data curation [supporting], formal analysis [supporting], investigation [supporting], writing – review & editing [supporting]), T.M. (Formal analysis [supporting], writing - review & editing [supporting]), D.K. (Formal analysis [supporting], investigation [supporting]), R.G-F. (Methodology [supporting]), A.F. (Methodology [supporting], writing – review & editing [supporting]), A.V. (Methodology [supporting], supervision [supporting], writing – review & editing [supporting]), R.B. (Methodology [supporting], software [supporting], supervision [supporting], writing – review & editing [supporting]), and T.V. (Conceptualization [lead], data curation [supporting], formal analysis [supporting], funding acquisition [lead], methodology [supporting], project administration [lead], resources [lead], supervision [lead], writing – original draft [lead], writing – review & editing [lead]).

Supplementary data

Supplementary data are available at NAR online.

Conflict of interest

The authors have no relevant financial or non-financial interests to disclose.

Funding

This study was supported by the German Research Foundation [SPP1378 (TV)] and [322977937/GRK2344 (TV)] and

by the Excellence Initiative of the German Research Foundation (GSC-4, Spemann Graduate School) (TV). Funding to pay the Open Access publication charges for this article was provided by the German Research Foundation in the framework of GRK 2344. RGF acknowledges the German Research Foundation support of GRK2606, project ID 423813989.

Data availability

RNAseq data after scRNAseq of cortical organoids (CO) from HD, FOXG1del, and FOXG1c460 were deposited to the NCBI Gene Expression Omnibus (GEO) with accession number GSE273180. Human FOXG1-ChIPseq from hCO were deposited to GEO with the accession number GSE272853. RNAseq data of E18.5 hippocampus and adult hippocampus were published previously [22, 24], and have the accession numbers GSE189119 (E18.5 hippocampus) and GSE106801 (adult hippocampus). E13.5 RNAseq data from cerebral cortex have the accession number GSE95833. RNAseq data from DIV7 primary hippocampal neurons with *Foxg1*KD and *Pantr1*KD were deposited to GEO with accession number GSE172220. Murine FOXG1-ChIPseq data after *Pantr1*KD in DIV7 primary hippocampal neurons were deposited to GEO with accession number GSE272852. RIPseq data were deposited to GEO with accession number GSE272854. NEUROD1 and FOXG1-ChIPseq data of DIV11 primary hippocampal neurons are published with accession number GSE189119 [22]. All other data types and codes recreating the analyses from the data files can be found at DOIs: 10.6084/m9.figshare.26788915 (https://figshare.com/s/bbff462c5689515bfb39) and 10.6084/m9.figshare.28869728 (https://figshare.com/s/97ba6960e2841fe9fe78) as R markdown files, Python scripts, and Galaxy workflows. The MS proteomics data from mouse N2a cells have been deposited to the ProteomeXchange Consortium via the PRIDE [60] partner repository with the dataset identifier PXD056060. The MS raw data for the hCO FOXG1 interactome have been deposited at the ProteomeXchange Consortium (http://proteomecentral.proteomexchange.org) under the accession number PXD062978. Furthermore, all MS proteomics datasets used and/or analysed during this study are available online at the MassIVE repository (http://massive.ucsd.edu/; dataset identifier: MSV000097629).

Ethics approval

All mouse experiments were approved by the animal welfare committees of the respective authorities (X-14/04H, X-17/03S and X-22/02B, Regierungspräsidium Freiburg, Germany).

References

1. Mitter D, Pringsheim M, Kaulisch M *et al.* FOXG1 syndrome: genotype-phenotype association in 83 patients with FOXG1 variants. *Genet Med* 2018;**20**:98–108. https://doi.org/10.1038/gim.2017.75
2. Mariani J, Coppola G, Zhang P *et al.* FOXG1-dependent dysregulation of GABA/glutamate neuron differentiation in Autism spectrum disorders. *Cell* 2015;**162**:375–90. https://doi.org/10.1016/j.cell.2015.06.034
3. Miyoshi G, Ueta Y, Natsubori A *et al.* FoxG1 regulates the formation of cortical GABAergic circuit during an early postnatal critical period resulting in autism spectrum disorder-like phenotypes. *Nat Commun* 2021;**12**:3773–17. https://doi.org/10.1038/s41467-021-23987-z
4. Xuan S, Baptista CA, Balas G *et al.* Winged helix transcription factor BF-1 is essential for the development of the cerebral hemispheres. *Neuron* 1995;**14**:1141–52. https://doi.org/10.1016/0896-6273(95)90262-7
5. Miyoshi G, Fishell G. Dynamic FoxG1 expression coordinates the integration of multipolar pyramidal neuron precursors into the cortical plate. *Neuron* 2012;**74**:1045–58. https://doi.org/10.1016/j.neuron.2012.04.025
6. Hou PS, Miyoshi G, Hanashima C. Sensory cortex wiring requires preselection of short- and long-range projection neurons through an Egr-Foxg1-COUP-TFI network. *Nat Commun* 2019;**10**:3581. https://doi.org/10.1038/s41467-019-11043-w
7. Cargnin F, Kwon J-S, Katzman S *et al.* FOXG1 Orchestrates neocortical organization and cortico-cortical connections. *Neuron* 2018;**100**:1083–1096.e5. https://doi.org/10.1016/j.neuron.2018.10.016
8. Brancaccio M, Pivetta C, Granzotto M *et al.* Emx2 and Foxg1 inhibit gliogenesis and promote neuronogenesis. *Stem Cells* 2010;**28**:1206–18. https://doi.org/10.1002/stem.443
9. Siegenthaler JA, Miller MW. Generation of Cajal–Retzius neurons in mouse forebrain is regulated by transforming growth factor β-Fox signaling pathways. *Dev Biol* 2008;**313**:35–46. https://doi.org/10.1016/j.ydbio.2007.09.036
10. Manuel MN, Martynoga B, Molinek MD *et al.* The transcription factor Foxg1 regulates telencephalic progenitor proliferation cell autonomously, in part by controlling Pax6 expression levels. *Neural Dev* 2011;**6**:9. https://doi.org/10.1186/1749-8104-6-9
11. Tian C, Gong Y, Yang Y *et al.* Foxg1 has an essential role in postnatal development of the dentate gyrus. *J Neurosci* 2012;**32**:2931–49. https://doi.org/10.1523/JNEUROSCI.5240-11.2012
12. Dastidar SG, Landrieu PMZ, D'Mello SR. FoxG1 promotes the survival of postmitotic neurons. *J Neurosci* 2011;**31**:402–13. https://doi.org/10.1523/JNEUROSCI.2897-10.2011
13. Shen L, Nam H-S, Song P *et al.* FoxG1 haploinsufficiency results in impaired neurogenesis in the postnatal hippocampus and contextual memory deficits. *Hippocampus* 2006;**16**:875–90. https://doi.org/10.1002/hipo.20218
14. Tigani W, Rossi MP, Artimagnella O *et al.* Foxg1 upregulation enhances neocortical activity. *Cereb Cortex* 2020;**30**:5147–65. https://doi.org/10.1093/cercor/bhaa107
15. Testa G, Olimpico F, Pancrazi L *et al.* Cortical seizures in FoxG1± mice are accompanied by Akt/S6 overactivation, excitation/inhibition imbalance and impaired synaptic transmission. *Int J Mol Sci* 2019;**20**:4127.https://doi.org/10.3390/ijms20174127
16. Yu B, Liu J, Su M *et al.* Disruption of Foxg1 impairs neural plasticity leading to social and cognitive behavioral defects. *Mol Brain* 2019;**12**:63. https://doi.org/10.1186/s13041-019-0484-x
17. Patriarchi T, Amabile S, Frullanti E *et al.* Imbalance of excitatory/inhibitory synaptic protein expression in iPSC-derived neurons from FOXG1+/− patients and in foxg1+/− mice. *Eur J Hum Genet* 2016;**24**:871–80. https://doi.org/10.1038/ejhg.2015.216
18. Siegenthaler JA, Tremper-Wells BA, Miller MW. Foxg1 haploinsufficiency reduces the population of cortical intermediate progenitor cells: effect of increased p21 expression. *Cerebral Cortex* 2008;**18**:1865–75. https://doi.org/10.1093/cercor/bhm209
19. Seoane J, Le H-V, Shen L *et al.* Integration of Smad and forkhead pathways in the control of neuroepithelial and glioblastoma cell proliferation. *Cell* 2004;**117**:211–23. https://doi.org/10.1016/S0092-8674(04)00298-3
20. Vezzali R, Weise SC, Hellbach N *et al.* The FOXG1/FOXO/SMAD network balances proliferation and differentiation of cortical progenitors and activates Kcnh3 expression in mature neurons. *Oncotarget* 2016;**7**:37436–55. https://doi.org/10.18632/oncotarget.9545

21. Kumamoto T, Toma K-i, Gunadi *et al.* Foxg1 coordinates the switch from nonradially to radially migrating glutamatergic subtypes in the neocortex through spatiotemporal repression. *CellReports* 2013;**3**:931–45.
22. Akol I, Izzo A, Gather F *et al.* Multimodal epigenetic changes and altered NEUROD1 chromatin binding in the mouse hippocampus underlie FOXG1 syndrome. *Proc Natl Acad Sci USA* 2023;**120**:e2122467120. https://doi.org/10.1073/pnas.2122467120
23. Dai S, Li J, Zhang H *et al.* Structural basis for DNA recognition by FOXG1 and the characterization of disease-causing FOXG1 mutations. *J Mol Biol* 2020;**432**:6146–56. https://doi.org/10.1016/j.jmb.2020.10.007
24. Weise SC, Arumugam G, Villarreal A *et al.* FOXG1 regulates PRKAR2B transcriptionally and posttranscriptionally via miR200 in the adult hippocampus. *Mol Neurobiol* 2018;**56**:1–14.
25. Craig-Mueller N, Hammad R, Elling R *et al.* Modeling MyD88 deficiency In vitro provides new insights in its function. *Front Immunol* 2020;**11**:608802. https://doi.org/10.3389/fimmu.2020.608802
26. Lancaster MA, Renner M, Martin CA *et al.* Cerebral organoids model human brain development and microcephaly. *Nature* 2013;**501**:373–9. https://doi.org/10.1038/nature12517
27. Gabriel E, Gopalakrishnan J. Generation of iPSC-derived Human brain organoids to model early neurodevelopmental disorders. *J Vis Exp* 2017;**122**:e55372. https://doi.org/10.3791/55372
28. Hebert JM, McConnell SK. Targeting of cre to the Foxg1 (BF-1) locus mediates loxP recombination in the telencephalon and other developing head structures. *Dev Biol* 2000;**222**:296–306. https://doi.org/10.1006/dbio.2000.9732
29. Erickson KR, Farmer R, Merritt JK *et al.* Behavioral and brain anatomical analysis of Foxg1 heterozygous mice. *PLoS One* 2022;**17**:e0266861. https://doi.org/10.1371/journal.pone.0266861
30. Younger S, Boutros S, Cargnin F *et al.* Behavioral phenotypes of Foxg1 heterozygous mice. *Front Pharmacol* 2022;**13**:927296. https://doi.org/10.3389/fphar.2022.927296
31. Grassi D, Franz H, Vezzali R *et al.* Neuronal activity, TGFbeta-signaling and unpredictable chronic stress modulate transcription of Gadd45 Family members and DNA methylation in the hippocampus. *Cereb Cortex* 2017;**27**:4166–81. https://doi.org/10.1093/cercor/bhx095
32. Kistenmacher S, Schwammle M, Martin G *et al.* Enrichment, characterization, and proteomic profiling of small extracellular vesicles derived from Human limbal mesenchymal stromal cells and melanocytes. *Cells* 2024;**13**:623. https://doi.org/10.3390/cells13070623
33. Chu C, Quinn J, Chang HY. Chromatin isolation by RNA purification (ChIRP). *J Vis Exp* 2012;**61**:e3912. https://doi.org/10.3791/3912-v
34. Miller SA, Policastro RA, Sriramkumar S *et al.* LSD1 and aberrant DNA methylation mediate persistence of enteroendocrine progenitors that support BRAF-mutant colorectal cancer. *Cancer Res* 2021;**81**:3791–805. https://doi.org/10.1158/0008-5472.CAN-20-3562
35. Afgan E, Baker D, Beek M *et al.* The galaxy platform for accessible, reproducible and collaborative biomedical analyses: 2016 update. *Nucleic Acids Res* 2016;**44**:W3. https://doi.org/10.1093/nar/gkw343
36. Love MI, Huber W, Anders S. Moderated estimation of fold change and dispersion for RNA-seq data with DESeq2. *Genome Biol* 2014;**15**:W3–W10. https://doi.org/10.1186/s13059-014-0550-8
37. Wu T, Hu E, Xu S *et al.* clusterProfiler 4.0: a universal enrichment tool for interpreting omics data. *Innovation (Camb)* 2021;**2**:100141.
38. Kolde R. pheatmap: Pretty Heatmap. R package version 1.0.12 (ed.), 2019. https://cran.r-project.org/web/packages/pheatmap/index.html
39. Blighe K, Rana S, Lewis M. EnhancedVolcano: publication-ready volcano plots with enhanced colouring and labeling. 2019. https://github.com/kevinblighe/EnhancedVolcano
40. Galaxy C. The galaxy platform for accessible, reproducible and collaborative biomedical analyses: 2022 update. *Nucleic Acids Res* 2022;**50**:W345–51.
41. Liao Y, Smyth GK, Shi W. featureCounts: an efficient general purpose program for assigning sequence reads to genomic features. *Bioinformatics* 2014;**30**:923–30. https://doi.org/10.1093/bioinformatics/btt656
42. van Heeringen SJ, Veenstra GJ. GimmeMotifs: a de novo motif prediction pipeline for ChIP-sequencing experiments. *Bioinformatics* 2011;**27**:270–1. https://doi.org/10.1093/bioinformatics/btq636
43. Wickham H. *ggplot2: Elegant Graphics for Data Analysis*. Springer, Cham, 2016.
44. Kuo CC, Hanzelmann S, Senturk Cetin N *et al.* Detection of RNA-DNA binding sites in long noncoding RNAs. *Nucleic Acids Res* 2019;**47**:e32. https://doi.org/10.1093/nar/gkz037
45. Cox J, Mann M. MaxQuant enables high peptide identification rates, individualized p.p.b.-range mass accuracies and proteome-wide protein quantification. *Nat Biotechnol* 2008;**26**:1367–72. https://doi.org/10.1038/nbt.1511
46. Ross-Innes CS, Stark R, Teschendorff AE *et al.* Differential oestrogen receptor binding is associated with clinical outcome in breast cancer. *Nature* 2012;**481**:389–93. https://doi.org/10.1038/nature10730
47. Cheffer A, Garcia-Miralles M, Maier E *et al.* DOT1L deletion impairs the development of cortical parvalbumin-expressing interneurons. *Cereb Cortex* 2023;**33**:10272–85. https://doi.org/10.1093/cercor/bhad281
48. Zutterling C, Todeschini AL, Fourmy D *et al.* The forkhead DNA-binding domain binds specific G2-rich RNA sequences. *Nucleic Acids Res* 2023;**51**:12367–80. https://doi.org/10.1093/nar/gkad994
49. Liuzzi G, Artimagnella O, Frisari S *et al.* Foxg1 bimodally tunes L1-mRNA and -DNA dynamics in the developing murine neocortex. *Development* 2024;**151**:dev202292. https://doi.org/10.1242/dev.202292
50. Armaos A, Colantoni A, Proietti G *et al.* catRAPID omics v2.0: going deeper and wider in the prediction of protein-RNA interactions. *Nucleic Acids Res* 2021;**49**:W72–9. https://doi.org/10.1093/nar/gkab393
51. Wang J, Xiang D, Mei S *et al.* The novel long noncoding RNA Lnc19959.2 modulates triglyceride metabolism-associated genes through the interaction with purb and hnRNPA2B1. *Mol Metab* 2020;**37**:100996. https://doi.org/10.1016/j.molmet.2020.100996
52. Chang KC, Diermeier SD, Yu AT *et al.* MaTAR25 lncRNA regulates the Tensin1 gene to impact breast cancer progression. *Nat Commun* 2020;**11**:6438. https://doi.org/10.1038/s41467-020-20207-y
53. Jeffs GJ, Meloni BP, Bakker AJ *et al.* The role of the Na(+)/Ca(2+) exchanger (NCX) in neurons following ischaemia. *J Clin Neurosci* 2007;**14**:507–14. https://doi.org/10.1016/j.jocn.2006.07.013
54. Bulstrode H, Johnstone E, Marques-Torrejon MA *et al.* Elevated FOXG1 and SOX2 in glioblastoma enforces neural stem cell identity through transcriptional control of cell cycle and epigenetic regulators. *Genes Dev* 2017;**31**:757–73.
55. Shi F, Hu J, Zheng P *et al.* LncRNA PANTR1 is associated with poor prognostic and suppresses apoptosis in glioma. *J Oncol* 2023;**2023**:8537036. https://doi.org/10.1155/2023/8537036
56. Van Nostrand EL, Freese P, Pratt GA *et al.* A large-scale binding and functional map of human RNA-binding proteins. *Nature* 2020;**583**:711–9. https://doi.org/10.1038/s41586-020-2077-3
57. Ray D, Laverty KU, Jolma A *et al.* RNA-binding proteins that lack canonical RNA-binding domains are rarely sequence-specific. *Sci Rep* 2023;**13**:5238. https://doi.org/10.1038/s41598-023-32245-9

58. Ottoz DSM, Berchowitz LE. The role of disorder in RNA binding affinity and specificity. *Open Biol* 2020;**10**:200328. https://doi.org/10.1098/rsob.200328
59. Pang Y, Liu B. DisoFLAG: accurate prediction of protein intrinsic disorder and its functions using graph-based interaction protein language model. *BMC Biol* 2024;**22**:3. https://doi.org/10.1186/s12915-023-01803-y
60. Perez-Riverol Y, Bai J, Bandla C *et al.* The PRIDE database resources in 2022: a hub for mass spectrometry-based proteomics evidences. *Nucleic Acids Res* 2022;**50**:D543–52. https://doi.org/10.1093/nar/gkab1038
61. Montes R, Romero T, Cabrera S *et al.* Generation and characterization of the human iPSC line PBMC1-iPS4F1 from adult peripheral blood mononuclear cells. *Stem Cell Res* 2015;**15**:614–7. https://doi.org/10.1016/j.scr.2015.10.009
62. Krefft O, Jabali A, Iefremova V *et al.* Generation of standardized and reproducible forebrain-type cerebral organoids from Human induced pluripotent stem cells. *J Vis Exp* 2018;**131**:e56768. https://doi.org/10.3791/56768

Received: October 8, 2024. **Revised:** April 30, 2025. **Editorial Decision:** May 20, 2025. **Accepted:** June 2, 2025